

ALPHA FOUNDATION FOR THE IMPROVEMENT OF MINE SAFETY AND HEALTH

Final Technical Report

Project Title: Early-Warning System Prototype Tests for Real-Time Safety Intervention and Optimum Ventilation Control Assistance

Grant Number: AFSTII4FO-81

Organization: Board of Regents, NSHE, obo University of Nevada, Reno (UNR)
1664 North Virginia Street
204 Ross Hall/Mail Stop 325
Reno, NV 89557-0240
Department of Mining and Metallurgical Engineering

Principal Investigator: George Danko, Ph.D., D.Sc., Professor, UNR
Phone: 775-784-4284
e-mail: danko@unr.edu

Contact Information: Tracy D. Wheeler, Research Administrator
Office of Sponsored Projects
e-mail: ospadmin@unr.edu
Phone: 775-784-4040
Fax: 775-784-6680

Period of Performance: January 1, 2019 through January 31, 2023
Budget closing deadline: April 30, 2023

Project participants: George Danko, PhD, PI, EWS model and software development, supervisor of project participants and coordination of research progress
Javad Sattarvand, PhD, Co-PI, signal analysis and Artificial Intelligence (AI) tools
Davood Bahrami, PhD, EWS software programmer, Emeritus Faculty, UNR.
Timothy Murphy, BS research assistant, documentation, data acquisition system
Hosein Hashemi (Kusha), PhD research assistant, data acquisition, signal processing

Industrial Partners: Ventsim-Howden, Australia
An operating Coal Mine, Australia
Nevada Gold Mining Company, Leeville, and Cortez Mine Operations

Acknowledgement/Disclaimer: This study was sponsored by the Alpha Foundation for the Improvement of Mine Safety and Health, Inc. (ALPHA FOUNDATION). The views, opinions and recommendations expressed herein are solely those of the authors and do not imply any endorsement by the ALPHA FOUNDATION, its directors and staff.

1.0 Executive Summary

Prototype tests of new software tools of an Early Warning System (EWS) has been successfully completed during the past four years. The EWS concept for preventive intervention of mining safety and health incidents was inceptioned and first tested in 2014-2015 in a prior research project funded also by the Alpha Foundation. The proof-of-principle test at that time used the native software tools in Ventsim, a commercially available mine ventilation and contaminant transport model.

The main goal of the follow-up work *was to develop a prototype EWS safety system and prove by tests its performance using Atmospheric Monitoring System' data collected real-time during operations from partner mines*. The new and innovative components of EWS to be tested were: (1) time expansion into the future from the real-time monitoring signals by forecasting in accelerated, simulation-time from the data to predict any likely event in the near future that may compromise safety; and (2) space expansion from the AMS locations into the entire mine, in order to evaluate safety at any critical working area, even at a place where no monitoring station were installed.

The spatial and temporal expansions require high-performance numerical simulation of the mine site real-time, synchronized with the mining operations to forecast in time and to expand in space model data to all locations of interest. For the tasks, we pursued a high-performance, Dynamic Mine Ventilation Model (DMVM) using the Multiflux code with advanced, time-dependent “thermal flywheel” simulation capabilities. Such dynamic model element is needed to analyze and forward-predict fast changes in temperature and contaminant concentrations.

A research partnership was formed between UNR and Ventsim Howden (previously Ventsim Chasm) to pursue the development of EWS and to link it to the most popular ventilation and contaminant modeling tool, used by over a thousand mining companies. New software components were needed to improve Ventsim's native models for time-dependent, dynamic simulations in accuracy and computational speed for real-time analysis. These new models of the EWS were included in the DMVM, linked to Ventsim's Graphical User Interface for model configuration setup.

On a parallel timeline, we also searched for applicable tools for EWS in Information Technology (IT), using ‘big data’, Machine Learning (ML), Artificial intelligence (AI), and Neural Networks (NN). Various Neural Network (NN) models were tested for signal trend analysis and forward prediction capabilities, obtaining moderate results with limited time gains (Dias et al., 2021; Dias, 2021). A refocused study experimenting with time series analysis and forward prediction resulted in improved AI models for real-time EWS applications [3]. A new, dynamic ML model was developed for e.g., barometric pressure-driven methane liberation prediction from the gob and the freshly cut face of the long-wall panel. The matrix operator of the model is determined from real-time AMS data from a partner mine by the automatic ML process, without user's input. The matrix operator can then be passed to the DMVM for forecasting methane liberation and concentration variations at the face in future time triggered by present, or future, forecasted barometric pressure variations. Similar to the dynamic methane liberation and concentration example, the matrix operator modeling tool is applicable to analyze and predict other hazardous atmospheric processes.

We received real-time AMS data from two operating mines for the research project: a few weeks of temperature, humidity, and gas concentrations data from a metal mine in Nevada; and a 327-day, continuous data from a full, long-wall panel extraction work from a coal mine in Australia. These data sets allowed us to evaluate the analytic and predictive capabilities of the EWS during normal mining operations.

Comparisons between measured AMS data from normal mining operations and simulated results from the DMVM model showed excellent agreements in test examples. Calibration of the DMVM model inputs were necessary when model inputs were not constrained sufficiently due to lack of prior data. Direct matching of the AMS data sets from the mines with various DMVM models showed that the EWS can assist in self-calibrating the DMVM model. Assisting in model input calibration by matching model output with measured data is an intuitive process supported by the EWS method. To wit, a root-cause analysis of a signal deviation (i.e., due to model boundary condition error) from expected value (i.e., AMS data) is analogous to self-calibration of the model for a specific input variable.

Synthetic hazard events were generated manually by perturbing the AMS signals for testing the forward prediction capabilities of the EWS software. We demonstrated by a series of numerical simulations that the DMVM and AI-ML elements of EWS can (a) recognize hazardous atmospheric conditions in their early evolution from AMS data; (b) find likely root causes for the event; (c) fast-forward-predict for likely outcomes of the root-cause problem; and (d) send a warning, triggered signal for preventive intervention of an impending malfunction or accident. The recognition of an upcoming hazard in its progression from (a) through (d) early on is the basis to prevent an impending accident.

In the last year of the project, we discovered that the root-cause analysis and the subsequent fast-forward prediction of an impending hazardous problem can be fused into a single process. The new, integrated AI process is triggered by any AMS signal's deviation from its normal range, followed by a fast-forward prediction of the AMS signal trend until it reaches and crosses the hazard threshold for prompting a warning message. The DMVM model elements are needed only for decomposing the possible input variables (such as, e.g., the air flow rate, the methane concentration at the main gate, the barometric pressure, and the root-cause methane liberation flux rate from the face and the gob) affecting the targeted output variable (such as, e.g., the output concentration of methane at the tail gate). After decomposition, a direct evaluation of the unknown root-cause of the methane liberation flux rate can be directly evaluated from the AMS signals by the ML, and AI processes continuously and real-time.

In summary, the prototype of the EWS software tools are completed and tested using a combination of DMVM, ML of the AMS signal and AI for triggering a warning message for acting with preventive measures before the observed, critical AMS signal may cross an accident threshold. The time gain depends on the changing rate of the AMS signal. In a moderately fast, deteriorating process with an evolution time of several hours, the time gain maybe about an hour in some examples (Danko, 2021; Danko, 2022). When the convolutional time series model is used for the identification of the contaminant transport system of the mine from AMS data, a prevention-focused engineering design may be used to achieve much larger time gains of several hours by triggering the EWS process by signals other than that of AMS, such as from weather forecast (Danko, 2022).

The results of the EWS project has been published (Dias et al., 2021; Danko, 2021; Danko, 2022), showing an overwhelming advantage of analyzing AMS data continuously and real time, to foresee safety and health hazards in their evolution for preventive interventions. The prototype tests were completed with the cooperation of Ventsim developers. Howden Ventsim is attentive in testing the EWS in operating mines and marketing it if interest from the mining industry or health and safety organizations is presented.

2.0 Problem Statement and Objective

The overall goal of the research project is to develop and test a prototype software of EWS for accident prevention by analyzing the mine's physical atmospheric system by preventive-focused engineering design as well as real-time AMS data using numerical simulation, ML and AI, followed by forecasting likely future outcomes of critical atmospheric conditions to safety and health. The input-output functional

components of EWS are linked to the GUI elements of Ventsim for easy setup of the configuration by the user.

Two complementary but equally recommended types of EWS applications were defined during project execution for mine safety and health improvements by preventive intervention measures:

(Type 1). Unexpected, real-time, preventive EWS intervention by the recognition of an accident-prone or health-hazard-prone atmospheric event, triggered by the analysis of the AMS signals;

(Type 2). Anticipated, model-prevented EWS intervention for any potential, accident-prone or health-hazard-prone atmospheric condition, determined by prevention-focused engineering design, triggered real-time by the analysis of a disturbing signal, either coming from the mine's AMS or from other signal (for example, weather forecast data).

Tasks in either (Type 1) or (Type 2) rely on the same EWS model and software tools. The input data handling to trigger the EWS is different in (Type 1) and (Type 2), requiring real-time AMS data handling in (Type 1), whereas a preparatory design analysis of the atmospheric system processes of the mine is needed for the task in (Type 2), in addition to real-time analysis of a mine-disturbing signal that may originate from data outside of the AMS of the mine (e.g., area weather data).

The specific goals of the development of the prototype EWS are to:

- Prove reliability of the experimental prototype EWS system using the AMS signals from commercial, approved monitoring sensors;
- Show the reliability and the self-calibration ability of the information system of the mine ventilation and contaminant concentration dynamic model including the DMVM component under operating conditions;
- Test the capability of fast forward prediction component in DMVM at any time triggered by any outside event or a request from the user to check for future threshold crossing within the EWS;
- Quantify the time advance for supporting intervention measures before the accident would have happened in emulated, what-if scenarios using off-line computer simulations for hypothetical, perceived, and relevant accident scenarios;
- Support mine management with output of real-time distress signal and accident-prone case definition for preventive intervention if imminent danger is recognized for mine safety;
- Provide a periodic summary chronicle or real-time report for safety factor variations with time at critical locations for health conditions;
- Provide a periodic summary chronicle or real-time report for under- or over-ventilation for supporting OVC and VOD control decisions.

3.0 Research Approach:

The study design include 10 tasks spread over the extended, four years of research period. The Atmospheric Monitoring System (AMS) layout of the mine is mapped in Ventsim Control in the GUI for connecting the sensor's locations to the DMVM for the mines. The unexpected (Type 1) EWS tasks are best supported by the current Ventsim Control software, whereas both Ventsim Control and Ventsim Design are needed to work in the anticipated (Type 2) EWS tasks.

The prototype EWS software is developed to analyze continuously real mine data in metal and coal mines. The EWS software uses the high-performance Multiflux solver for the DMVM model elements for matching mine data and predicting future simulated outcomes. The DMVM is designed with the cooperation of the Ventsim software development team under a partnership agreement to work with Ventsim Visual using its Graphical User Interface (GUI).

Continuous developments in the Ventsim Design software has improved the native solver tools both in accuracy and speed. Most of the additional functions needed in the EWS are currently supported by Ventsim Design, except for the enhancements included in the EWS such as the DMVM and the AI model components. The DMVM model elements are still needed for the short-time dynamic simulations, for example, for diurnal temperature and concentration variation predictions. For prevention-focused engineering design in Type 2 applications, the EWS uses a convolutional time series ML-AI model for the identification of the contaminant transport system of the mine from real-time AMS data, imported for from the database of Ventsim Control.

The calibrated DMVM model extends the EWS applicability to the entire mine airway system by creating DMVM simulation data for mine areas where AMS data are not available. For the unmonitored areas, the EWS uses the real-time DMVM model output data for safety and health analysis in the same manner the EWS is used in the monitored locations.

The primary function of EWS is to support preventive safety and health management. The additional benefits of EWS is cost savings in ventilation design and control. The EWS is well suited to be part of Ventsim Control for continuously analyze the AMS data stream and enhance it using the model-based, forward-in-time output information to evaluate health-affecting atmospheric conditions at any critical location and time in a mine.

EWS is aimed at providing support data to safety and health management to operate a mine according to Optimized Ventilation Control (OVC) by optimizing safety, health, and cost benefits if desired, now part of Ventsim Control. In addition, a mine may use the output data from the EWS for Ventilation on Demand (VOD) control if desired, always keeping the operation safe and economical at any location and time, also a task delegated to the basic function of Ventsim Control.

Task 1. Complete the EWS Framework.

The work continued for three years on Task 1, described in detail in interim reports and summarized in Appendix 1.

a. GUI elements of the EWS

The GUI elements of the EWS linked to Ventsim Design and Ventsim Control are listed and shown in Figure 1.

The planning was completed for the functions of each EWS element and GUI component in preparation for the on-site discussion with the Ventsim Developers for EWS integration in parts A through F as follows. (Note the modification of Figure 1 from that in the 2019 Annual Report by the addition of Ventsim Design and the removal of Ventsim Live after the onsite work with the Ventsim Developers.)

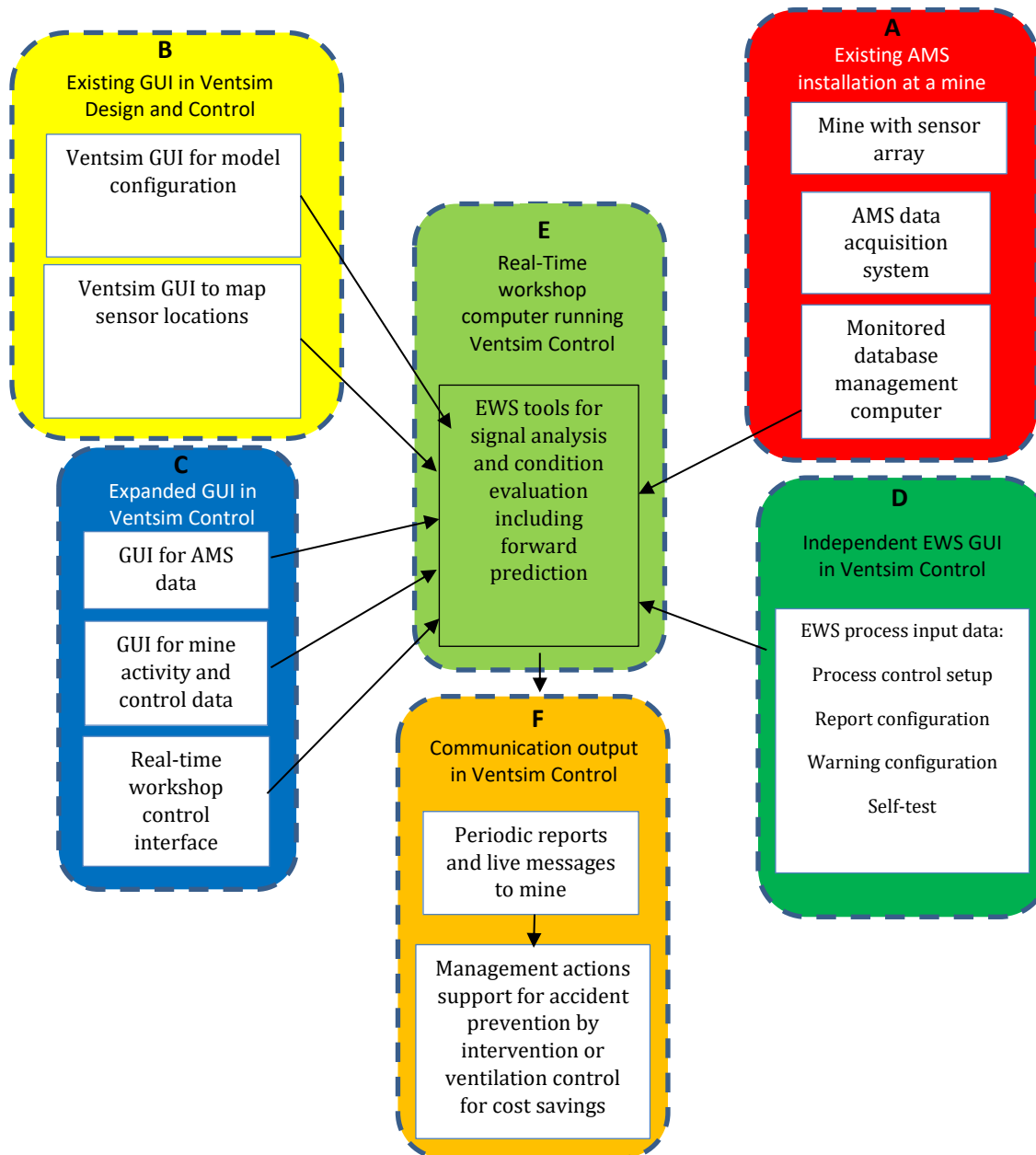


Figure 1. The description of the GUI elements of the EWS linked to Ventsim Design and Ventsim Control.

b. Data and Hardware configuration of the EWS

The design layout of the EWS, the basic data flow and hardware components are shown in Figure 2.

c. AMS network mapping to EWS.

The conceptual data flow configuration of the EWS is shown in Figure 3.

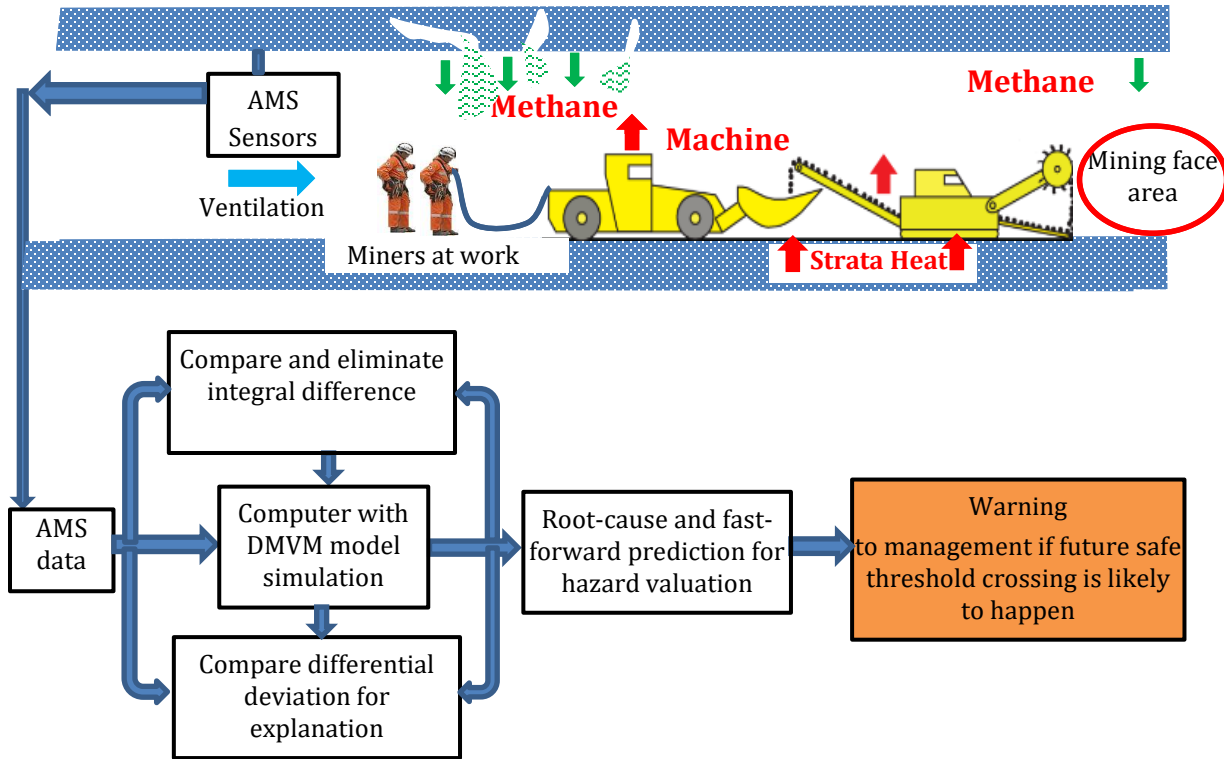


Figure 2. The design layout of the EWS with its basic data flow and hardware components.

Task 2. The DMVM software in MULTIFLUX (MF).

The work continued for four years on Task 2 with developments and tests, described in detail in interim reports and summarized in Appendix 1.

a. Dynamic model elements and configurations for air flow, heat, moisture, and contaminant concentration.

The DMVM model in MF, its link to Ventsim Design, and comparisons are published in open-access journal article (Danko et. al, 2020). Recent DMVM improvements are explained in Appendix 1. The DMVM model linkage and calibration against AMS data streams are shown in Appendix 2. The results of a comparison example between the DMVM model and Ventsim simulation is shown with excellent match in Appendix 3.

b. The gob model.

Examples of model tests were carried out for methane concentration simulations in various stages during mining operation in the entire long wall panel. Figure 4 shows the layout geometry of the full gob at day 327 of the completed mining operation.

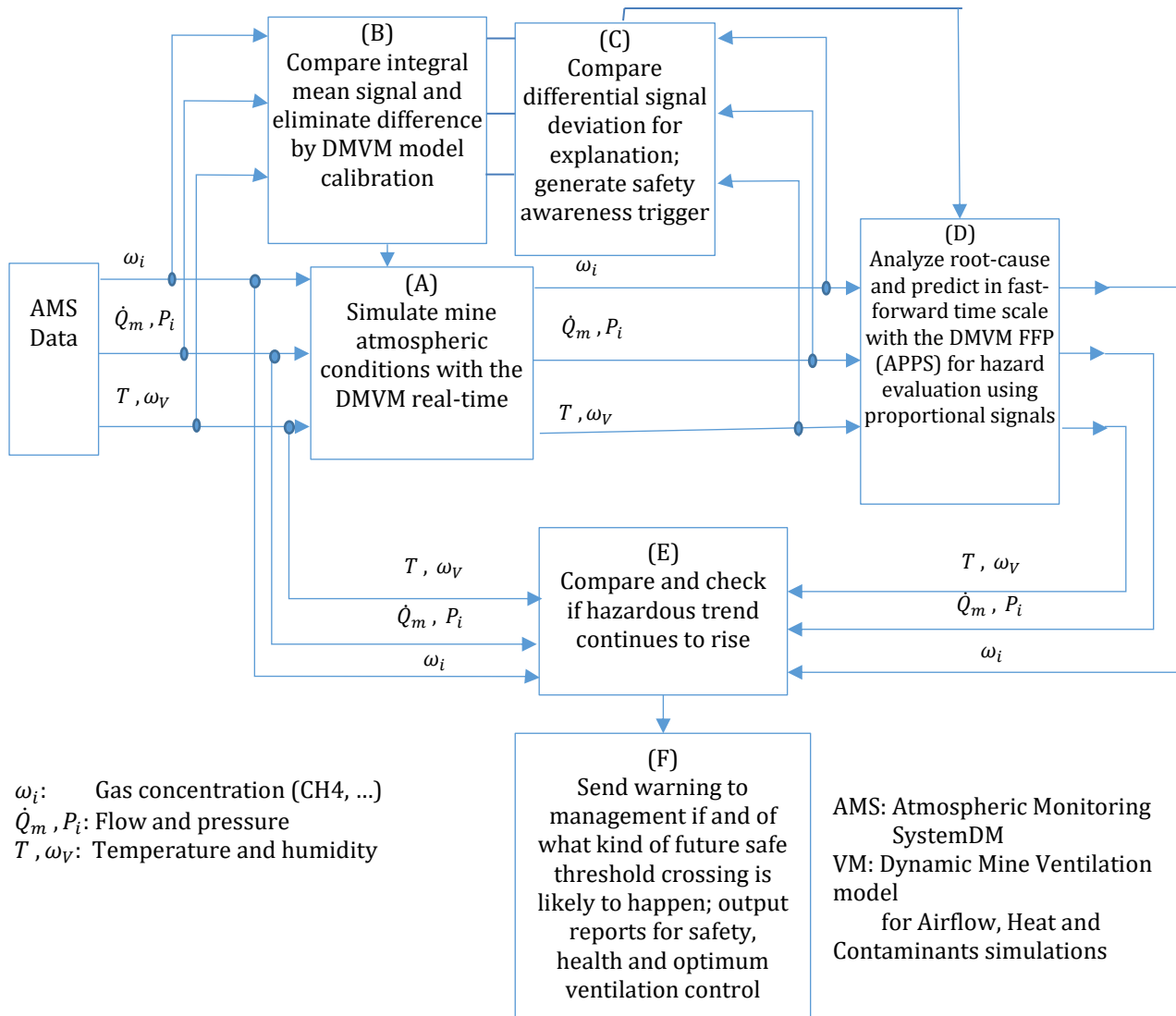


Figure 3. The conceptual data flow configuration of the EWS.

Task 3. The DMVM Model Calibrator.

The work continued between years 2 and 3 on Task 3 as described in detail in interim reports and summarized in Appendix 1.

a. DMVM model calibration processes. Examples of model calibration.

Automatic, self-calibration processes were developed and tested based on matching AMS data trends with DMVM model predictions. Figures 5-7 show DMVM self-calibration tests examples at various locations at the moving the shearer's gate and in the gob. Figure 8 shows the evaluation results of the root cause of methane concentration variations at various points in the longwall panel, related to Figures 5-7 in terms of methane mass fluxes in the upstream airflow segments.

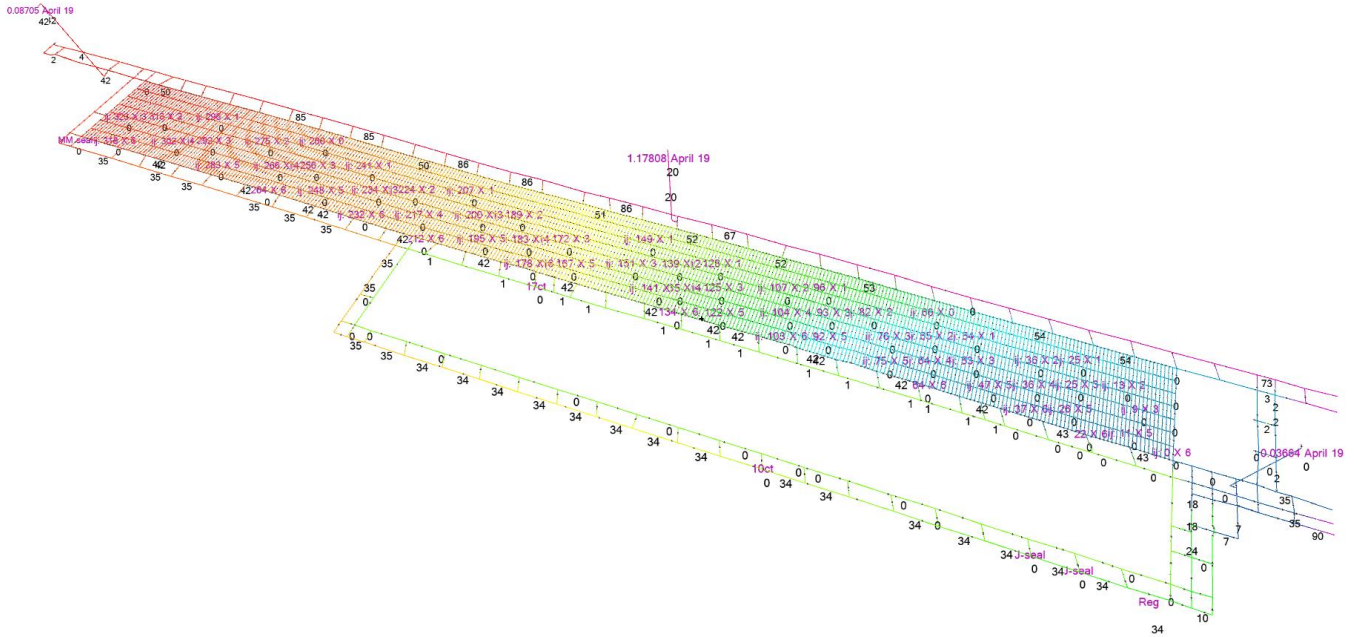


Figure 4. A longwall panel of a coal mine partner's mine discretized for gob modeling (309.7m x 3,822m, with 7 x 327 internal grid lines) in the DMVM model in Ventsim.

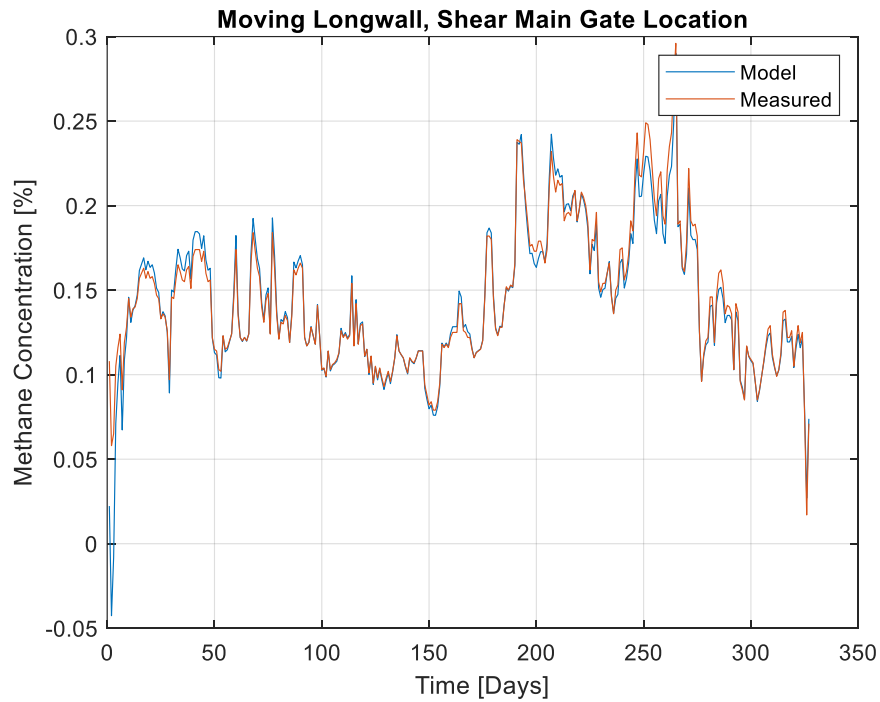


Figure 5. Self-calibrated, simulated, and measured Methane concentrations at the Main Gate (MG) location in the longwall panel (the shearer location moves over 1 through 3,687 m in 327 days).

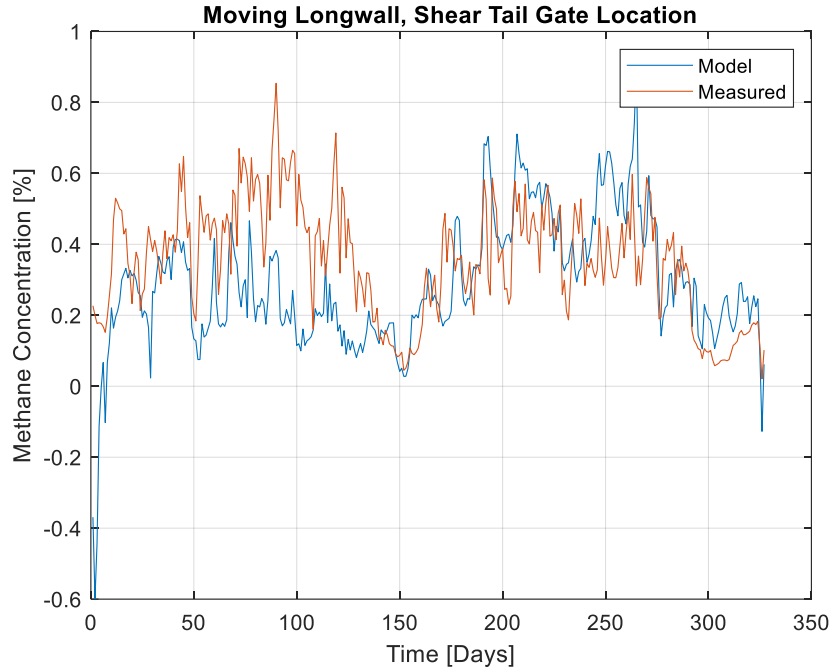


Figure 6. Self-calibrated, simulated, and measured Methane concentrations at the Tail Gate (TG) location in the longwall panel (the shearer location moves over 1 through 3,687 m in 327 days).

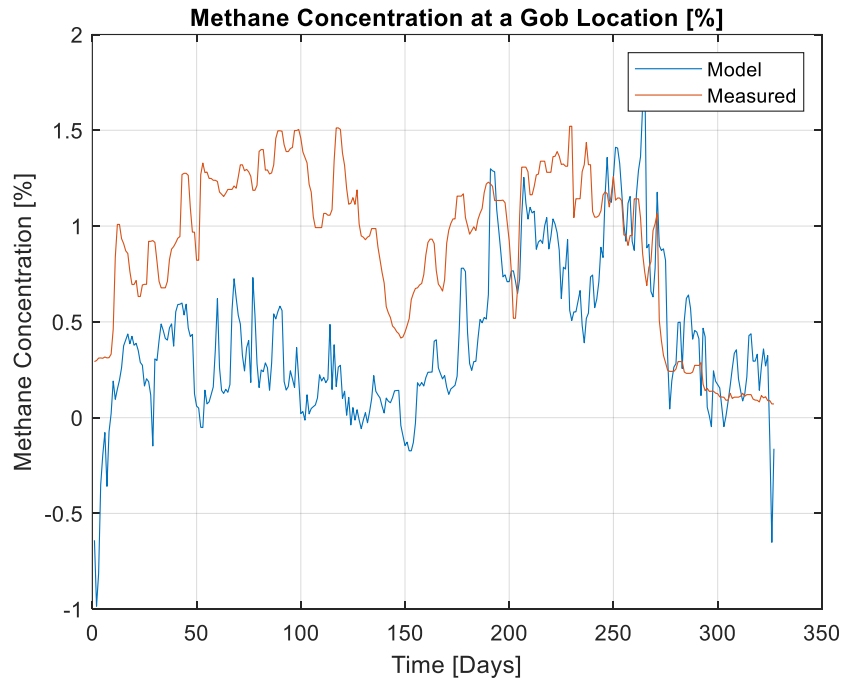


Figure 7. Self-calibrated, simulated, and measured Methane concentrations at a gob location close to the longwall panel exit end (the shearer location moves over 1 through 3,687 m in 327 days).
(MG , TG, and Panel Exit locations)

Task 4. **Safety awareness signal processor.**

Signal pattern recognition method developments with ML, AI, and NN models continued between years 2 and 4 on Task 4 as published (Dias, 2021, Dias et. al, 2021) and reported in the interim reports with results and conclusions. The developments and tests are summarized in Appendix 1.

a. AMS signal patterns recognition.

Signal pattern recognition methods were planned, developed and tested in examples using saved, real-time data for 327 days from AMS of an operating coal mine in Australia. The narxnet-type NN was used in the first tests. The input data from AMS were flow rate, barometric pressure, and methane concentration at the MG location. The model target was the methane concentration variation at the TG location at a future time as a function of the input data variations over a past time interval of 50 days. For NN model training, a sliding window-type progression was used. Data from 1 to 50 time steps were used to learn methane concentration at the TG one time step (one day) ahead from the input variations. Figure 8 shows the comparison of the predicted and the measured methane concentrations over 270 sliding window predictions. As depicted, the one-day forward prediction from the NN model fails to follow well the measured concentration variation. Instead of forecasting with time gain (even for only one day), a time delay is seen of several days in the predicted concentration; and nearly all concentration spikes were missed by the NN model.

The NN narxnet models were further studied analyzing AMS data from a metal mine in Nevada. A few weeks of recorded, real-time AMS data were used to train over 8000 minutes temperature samples to predict the temperatures during the following 2000 time steps. Examples are shown for training and prediction performances in Figures 9 and 10 for two different sensor locations, depicting poor forecasting performance.

Several other types of NN models were tested over three years with various results, but none significantly favorable for EWS application, published in an international conference (Dias et al., 2021) and in an M.S. thesis (Dias, 2021).

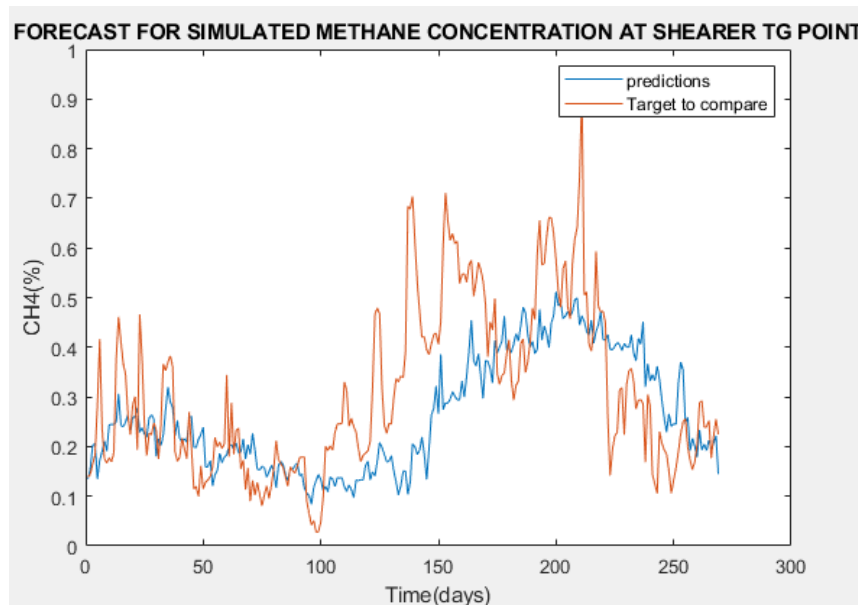


Figure 8. Comparison of measured and predicted concentrations from a NN model.

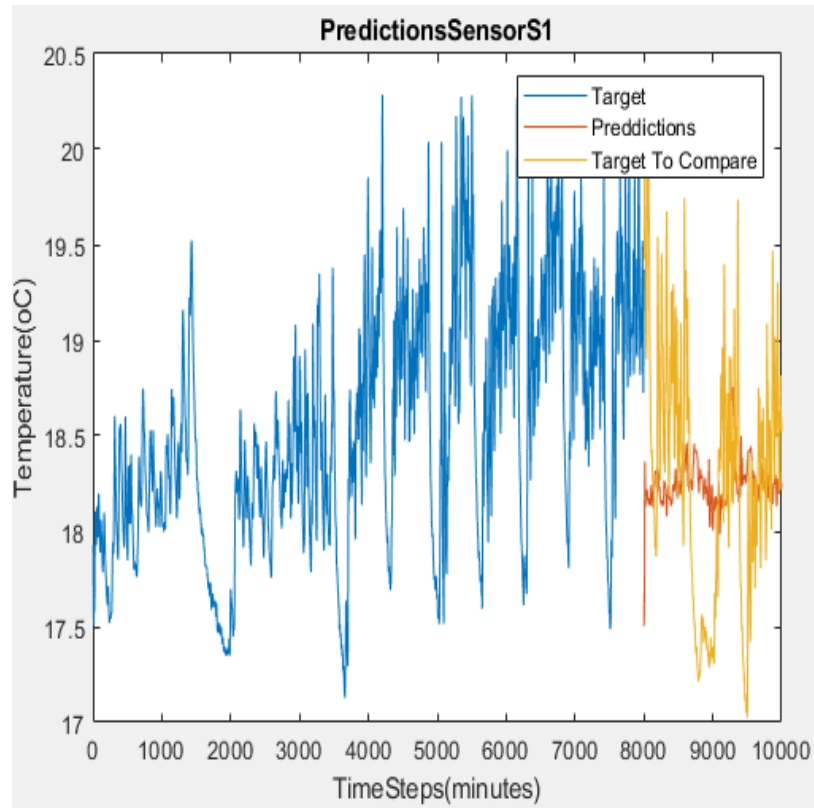


Figure 9. NN model's training and prediction for air temperature variations at sensor 1 location.

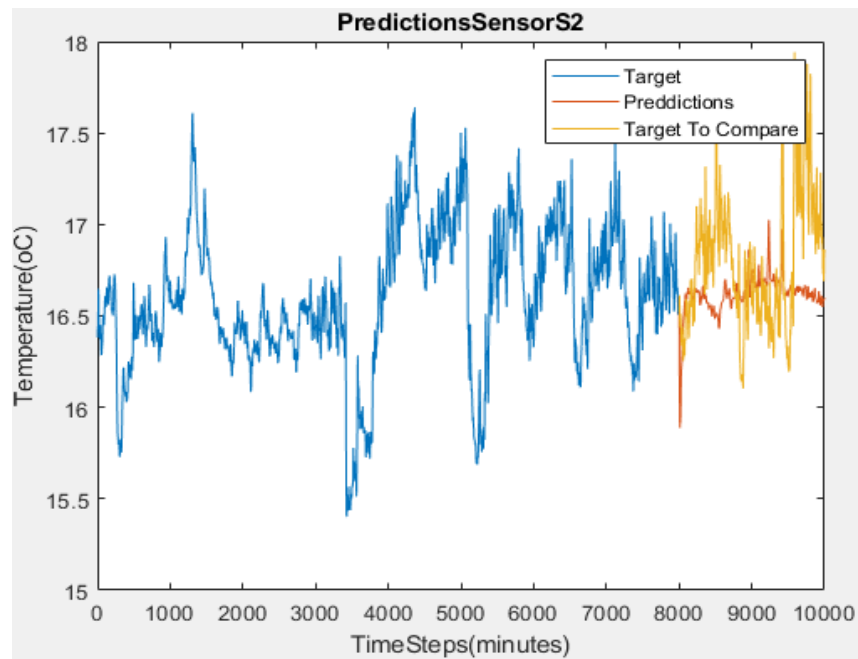


Figure 10. NN model's training and prediction for air temperature variations at sensor 2 location.

b. Analysis of AMS trends.

To surpass the failed NN models, new methods were considered, designed, developed, and tested for real-time EWS applications over the years 2 through 4.

A new dynamic model identification method was developed for continuous time series analysis and forward prediction applications. Quantum of data was defined over moving time intervals in sliding window coordinates for compressing the size of stored data while retaining the resolution of information. Quantum vectors formed the basis of a linear space for defining a dynamic quantum operator (DQO) model of the system defined by its data stream. The transport of the quantum of compressed data was modeled between the time interval bins during the movement of the sliding time window. The DQO model was identified from the samples of the real-time flow of AMS data over the sliding time window. A least-square-fit identification method was developed for evaluating the parameters of the quantum operator model, utilizing the repeated use of the sampled data through a number of time steps. The method was tested to analyze, and forward-predict air temperature variations accessed from weather data as well as methane concentration variations obtained from measurements of an operating coal mine in Australia. The results showed efficient forward prediction capabilities, surpassing those using neural network and other methods for the same task.

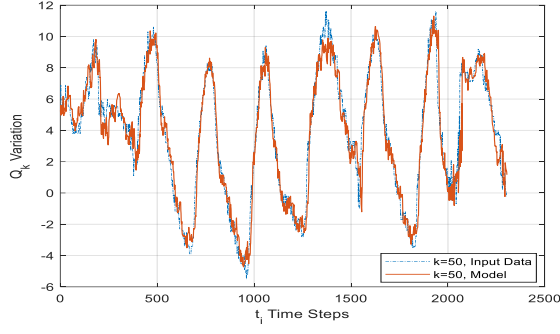
Only a few examples are selected in the report from the full, open-access publication of the DQO model (Danko, 2021) for illustrative purposes. Temperature data for 327 days were sampled at regular 5-minute time intervals for quantum-processing described in the referenced publication for a model fitting and prediction exercise. At each of the $i = 1$ to 327×288 time steps, a separate DQO model was built using four days with sliding window width, $w = 8 \times 288 = 2304$ as set S . The goals of the exercise were to check the quality of (a) the DQO model fit for each time step, measured by the normalized absolute error between input data and model prediction at each time step; and (b) the DQO forward prediction steps of $z = 12$ steps ahead at each time step, measured by the normalized absolute error between the known (but yet unused) input data at $i + z$ and the model forward prediction at $i + z$ time step. The sliding time window was moved from $i = 1$, starting from an initial assumption of all zero history quantum values. The DQO model was trained to match the last 20 quantum components only (for $k \in [31, 50]$) as just a short memory of the system was needed to learn for a $z = 12$ -step forward prediction.

After the 400 coefficients of the ϕ^S matrix of the DQO model were determined from a least-square-fit (LSQ) scheme at each i time step (where $i \in S$, and S is the set of a sufficiently large data set for a unique LSQ solution), the model prediction, Q_M^i , was calculated from the quantum-processed input data Q_D^{i-z} taken at back-shifted time instants as:

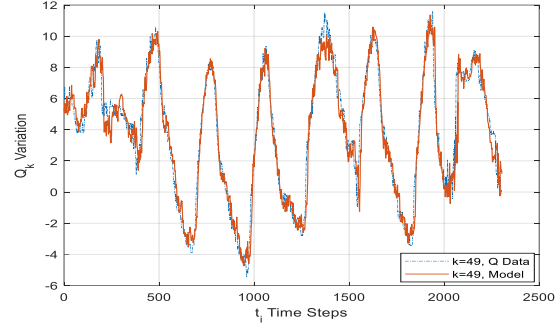
$$Q_M^i = \phi^i Q_D^{i-z} \quad (1)$$

The variation of the measured data Q_D^i and modeled Q_M^i quantum vector components for the $k \in [31, 50]$ components for the last moving window segment for $i \in S$ are shown in Figures 11 a-h. The components of the Q_M^i and Q_D^i vectors with time are shown in (a)-(g) for $k \in [44, 50]$ (with each individual pair and k marked); and in (h) for $k \in [31, 43]$ (with only each k marked as no difference between Q_D^i and Q_M^i can be seen). Note that Figure 12 a shows the DQO model match to the 5-minute data as the quantum vector for $k = 50$ equals the un-processed input data. As shown in Figures 11 a-h, the match between the DQO model's output results, Q_M^i , and the input data, Q_D^i , is gradually improving toward slower frequency components at decreasing k values.

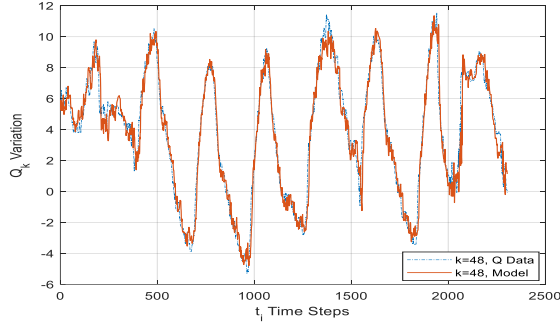
The normalized absolute error of the model fit for each time step over each sliding window $w = 2304$ is calculated as $E(i)$ for $i = 1$ to 327×288 time step (327 days):



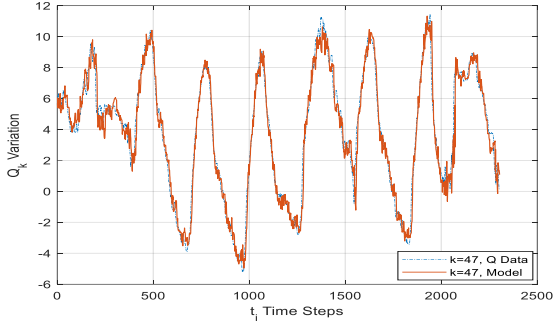
(a)



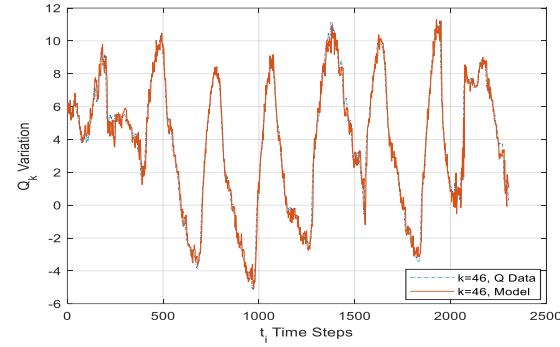
(b)



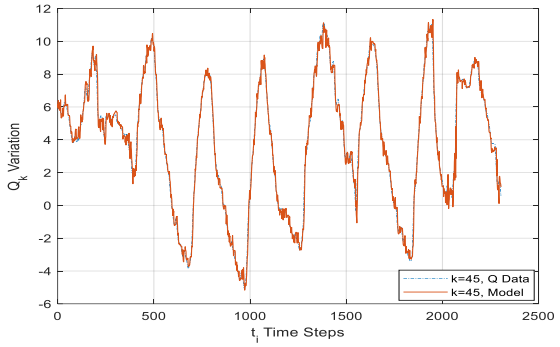
(c)



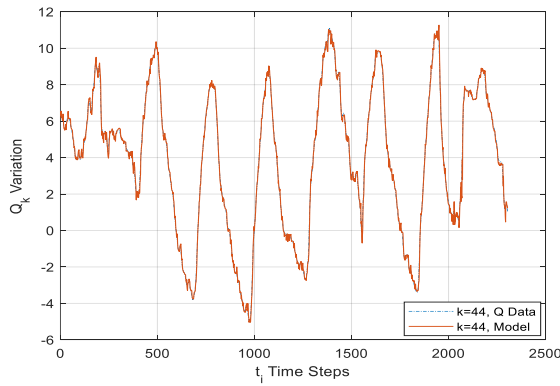
(d)



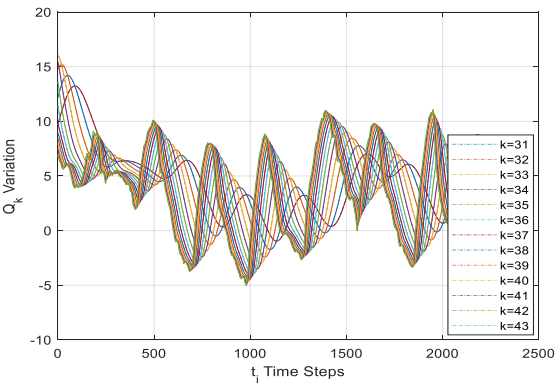
(e)



(f)



(g)



(h)

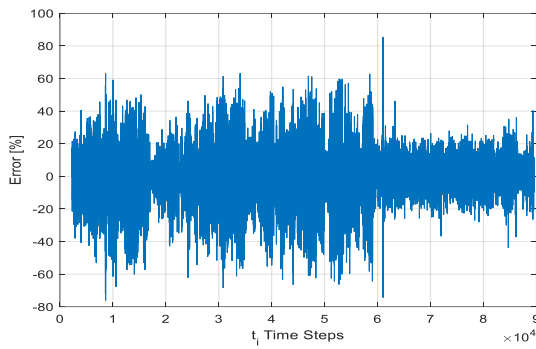
Figures 11 a-h. Variation of the \mathbf{Q}_M^i and \mathbf{Q}_D^i vectors with time for input data series from measurement; (a)-(g): $k \in [44, 50]$ (with each individual pair and k marked); (h): $k \in [31, 43]$ (with only each k marked as no difference I between \mathbf{Q}_D^i and \mathbf{Q}_M^i can be seen).

$$E(i) = \frac{w(Q_M^i - Q_D^i)}{\sum_{j=1}^w |Q_D^{i-j+1}|} 100 \quad [\%] \quad (2)$$

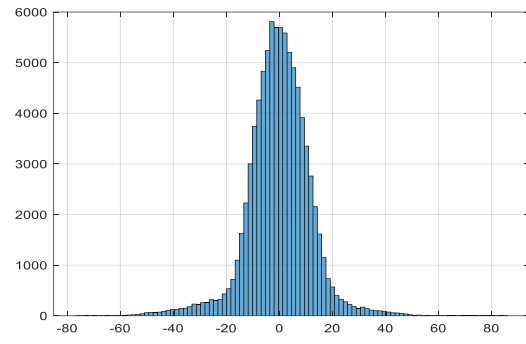
The normalized absolute error of the model fit at forward predicted instances by z time steps for each time step over each sliding window $w = 2304$ is calculated as $E_z(i)$:

$$E_z(i) = \frac{w(Q_M^{i+z} - Q_D^{i+z})}{\sum_{j=1}^w |Q_D^{i-j+z-1}|} 100 \quad [\%] \quad (3)$$

The graphs of $E(i)$ and $E_z(i)$ are shown in Figures 12 a, b and 14 a, b for the temperature; and in Figures 16 a, b and 18 a, b for the methane concentration examples, respectively.



(a)



(b)

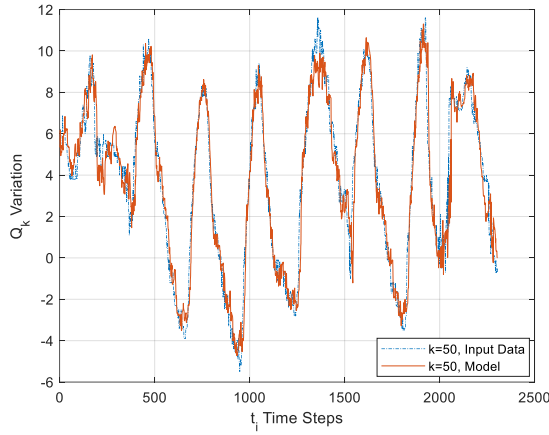
Figures 12 a, b. Variations of normalized absolute DQO model error; (a) Model error over the training time window, $E(i)$; and (b) Histogram of the model error.

The forward-predicting capability of the DQO model was tested by evaluating forecasted outputs from previous known values. This was accomplished by calculating the model's output ahead by $z = 12$ time steps outside the training time window, while using a 12-step old DQO:

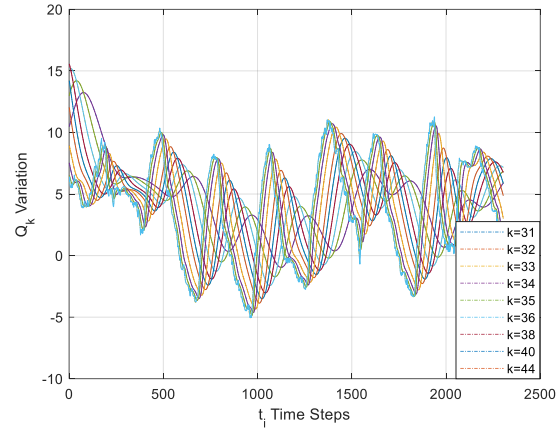
$$Q_M^{i+z} = \phi^i Q_D^i \quad (4)$$

Figures 13 a, b show the variation of selected Q_M^{i+z} and Q_D^{i+z} vectors over the entire last training window forward predicted by z time steps, compared with input data series from measurement. The components of the Q_M^{i+z} and Q_D^{i+z} vectors with time are shown in (a) for $k = 50$ (with marked pairs of Q_D^{i+z} and Q_M^{i+z}); and in (b) for $k \in [31, 44]$ (with only each k marked as no difference between model and data can be seen). As shown in Figures 13 a and b, the match between the DQO model's output results, Q_M^{i+z} , and the input data, Q_D^{i+z} , is about as good as the match before, indicating that input data have a learnable trend that holds well for about an hour ahead.

A comparison between Figures 12 and 14 indicates a steady error performance in forward prediction application relative to that in model identification. A stable DQO model performance up to 12 forward-step forecast in the example makes the method appealing, especially in comparison to published results for LSTM NN models with poorer forward prediction performance (Dias et al., 2021).



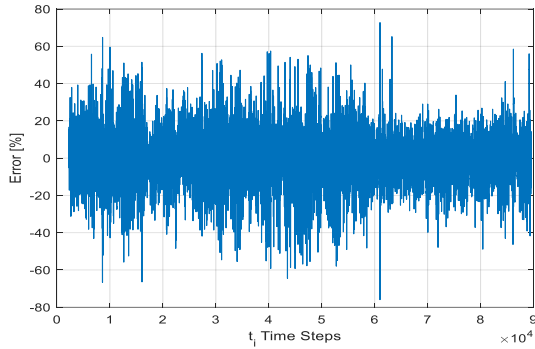
(a)



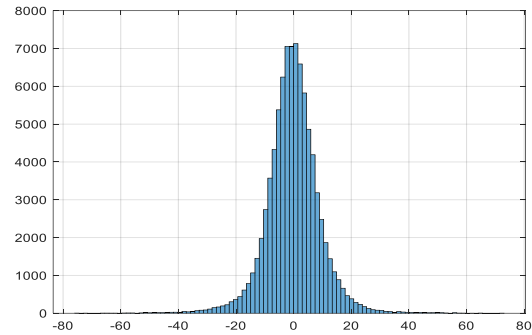
(b)

Figures 13 a, b. Variation of selected Q_M^{i+z} and Q_D^{i+z} vectors forward predicted by $z = 12$ time steps, compared with input data series from measurement; (a): $k = 50$ (with marked pairs of Q_D^{i+z} and Q_M^{i+z}); (b): $k \in [31, 44]$ (with only each k marked as no difference between model and data can be seen).

The graphs of $E(i)$ and $E_z(i)$ for forward prediction are shown in Figure 15a and b, respectively.



(a)

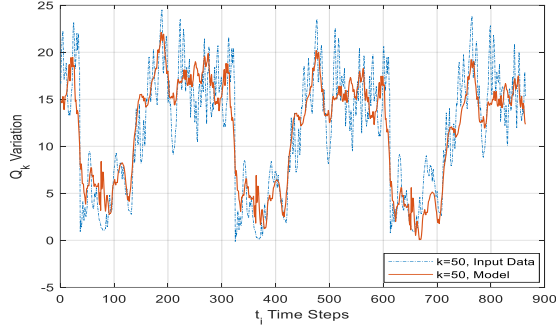


(b)

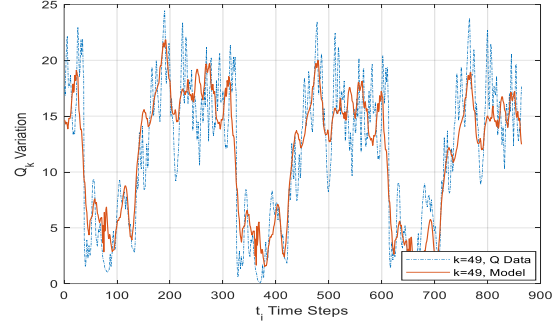
Figures 14 a, b. Variations of normalized absolute DQO model error; (a) Model error at 12 time steps (60 minutes) forward, $E_{fps}(i)$; and (b) ; and (b) Histogram of the model error.

In the coal mine example, the second-sampled AMS data stream from the TG methane sensor was first resampled every 5 minutes by sliding window averaging every 300 consecutive data samples. The reduced data set included 288 data points each day for air flow rate, (Qa), barometric pressure, (Pb), and each gas concentration component from the mine, e.g., methane (CH_4) at the MG, TG, gob, and near Panel Exit points.

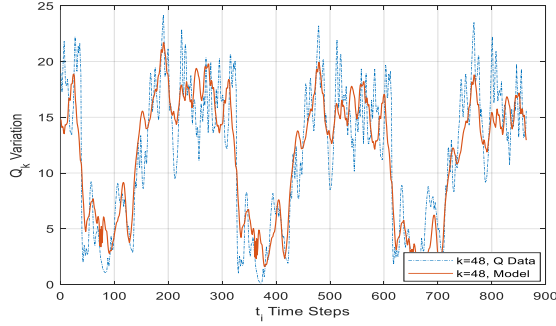
Each parameter was processed first into quantum vector, and then modeled continuously with DQO with time over 327 days. The Q vectors' size was kept 50 in the examples. The variation of the measured data Q_D^i and modeled Q_M^i quantum vector components for the $k \in [31, 50]$ components for the last moving window segment for $i \in S$ are shown in Figures 15 a-h. Figures 16 a and b illustrate the normalized fitting error and its hysteresis curve between measured and modeled methane concentrations from the DQO model, repeated over 320 days (89,000 5-minute time steps).



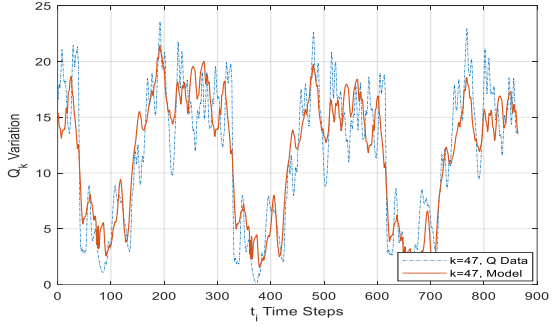
(a)



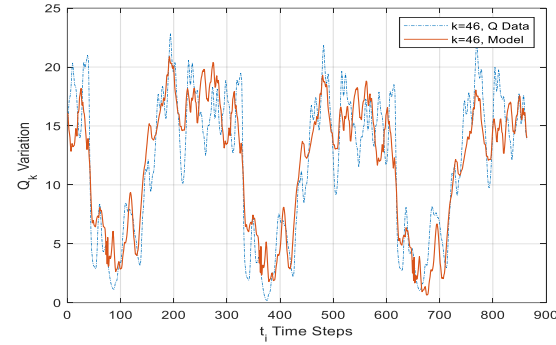
(b)



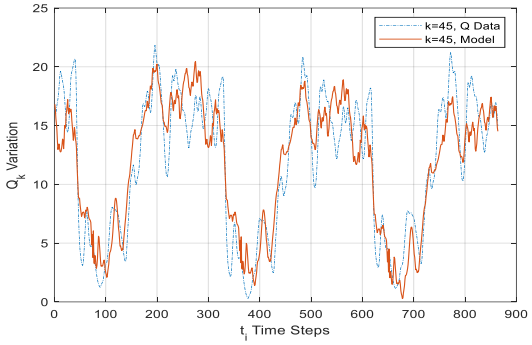
(c)



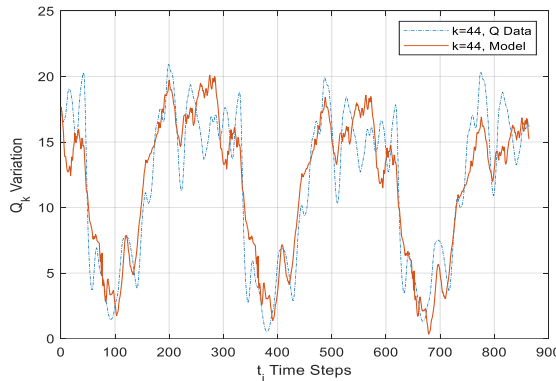
(d)



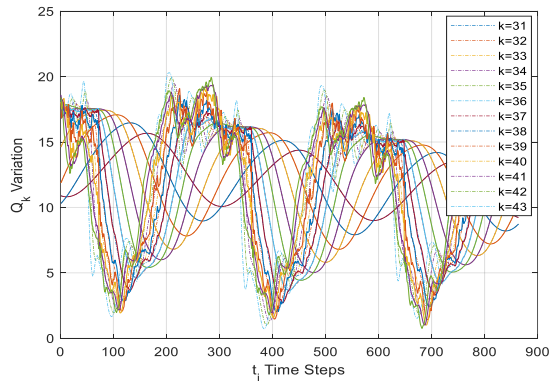
(e)



(f)

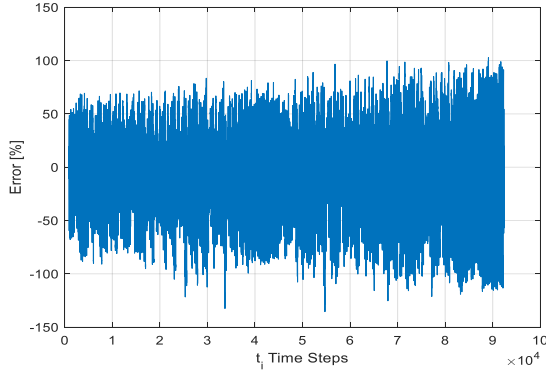


(g)

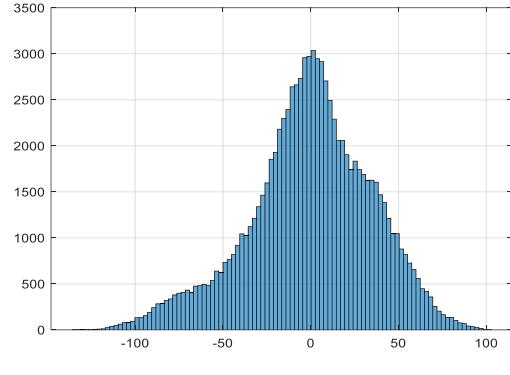


(h)

Figures 15 a-h. Variation of the Q_M^i and Q_D^i vectors with time for methane source input data series from measurement; (a)-(g): $k \in [44, 50]$ (with each individual pair and k marked); (h): $k \in [31, 43]$ (with only each k marked as no difference between Q_D^i and Q_M^i could be seen).



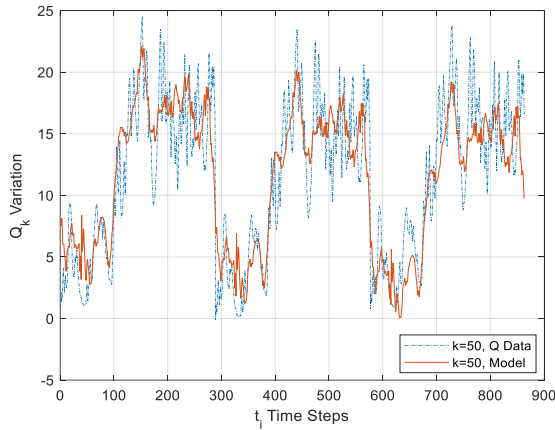
(a)



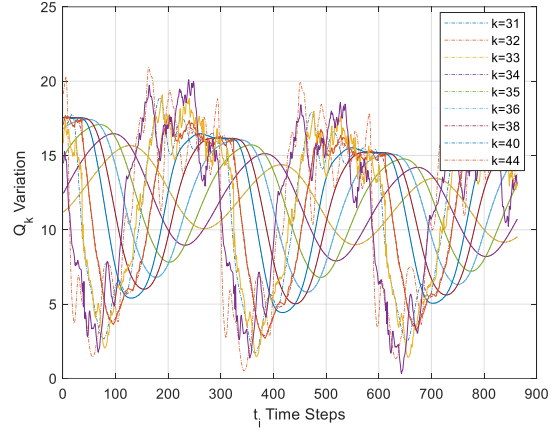
(b)

Figures 16 a, b. Variations of normalized absolute DQO model error for methane source; (a) Model error over the training time window, $E(i)$; and (b) Histogram of the model error.

The forward prediction capability of the DQO model was tested similar to that of the temperature model. Figures 16 a-h show the variation of selected \mathbf{Q}_M^{i+z} and \mathbf{Q}_D^{i+z} vectors forward predicted by $z=36$ time steps, compared with input data series from CH₄ source measurement. Figures 18 a and b illustrate the normalized fitting error and its hysteresis between measured and modeled methane concentrations from the DQO model, repeated over 320 days (89,000 5-minute time steps).

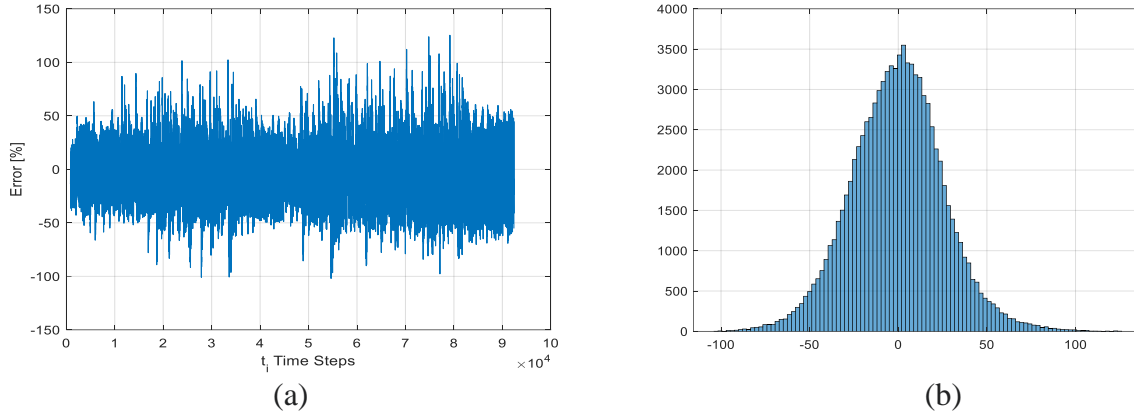


(a)



(b)

Figures 17 a, b. Variation of selected \mathbf{Q}_M^{i+z} and \mathbf{Q}_D^{i+z} vectors forward predicted by $z=36$ time steps, compared with input data series from CH₄ source measurement; (a): $k=50$ (with marked pairs of \mathbf{Q}_D^{i+z} and \mathbf{Q}_M^{i+z}); (b): $k \in [31, 44]$ (with only each k marked as no difference between model and data can be seen).



Figures 18 a, b. Variations of normalized absolute DQO model error for CH₄; (a) Model error for $z = 36$ time steps (180 minutes) forward prediction, $E_z(i)$; and (b) Histogram of the model error.

Note that DQO model identification is based on self-correlating current and past data samples, therefore it inherently includes a single time step. Forward prediction from DQO thus comes naturally by increasing the number of time steps, z (e.g., $z = 12$ in the temperature and $z = 36$ in the methane concentration example). As shown in illustrative examples published in detail (Danko, 2021) and summarized in Figures 11 through 18, the quality of DQO model identification performance is within about $\pm 60\%$ normalized error for the temperature prediction (for $z = 12$), and $\pm 100\%$ normalized error for the methane prediction cases (for $z = 36$). These error ranges mean that the predicted results are well bounded and can be reliably used for hazard warning, considering that a reduced EWS trigger level to half of the accepted safety value can easily compensate for a maximum of 100% prediction error.

The successful tests of the DQO model in the EWS for up to 1 hour forward-step forecast for temperature forecast and 3 hours for methane forecast makes the method appealing, especially in comparison to published results for NN models with poorer forward prediction performance for only one forward step. In addition to excellent stability, the computational time for model DQO identification and forward prediction at each time step takes 18 milliseconds using a laptop computer.

Task 5. The Root-Cause Evaluator in the EWS.

Signal processing and root-cause evaluation of signal change studies continued between years 2 and 4 in Task 5 as reported in the interim reports with results and conclusions. The developments and tests are summarized in Appendix 1.

a. Signal processing methods and root-cause evaluation of source terms in the DMVM for recognizing regular or hazardous patterns in the AMS signals.

Note that for normal mining operations, the AMS data based root-cause evaluation and automatic, self-calibration processes share the same mathematical techniques. DMVM self-calibration tests examples shown in Task 3 illustrate the success of the combined application AMS signal with the ventilation model in Figures 5-7 at various locations at the moving the shearers gate and in the gob.

Other results shown in Figures 1 and 13 for temperature and Figures 15 and 16 for methane concentration examples demonstrate the success of the DQO model to capture the dynamics of a set of data for a sizable time period from past to present time over a sliding window. This makes the DQO model a useful tool for root cause evaluation from real-time data.

For heat or methane (or any other) inflow source identification, a DQO model can be directly identified from AMS data for the expressed source term, formulated in DMVM for the critical part of the mine ventilation section (Danko, 2021). The advantage of identifying a root-cause source term by a DQO model directly from AMS data comes from DQO's ability for instantaneous forward prediction of expected future root-cause source term (heat and methane influx to the air in the examples). With the expected source term, the DMVM solution can instantly provide the expected future signal level (temperature and methane concentration in the examples).

b. Root-Cause evaluation of model conditions and source terms in the DMVM for mine safety design.

Understanding the root cause of hazardous conditions in a mine requires deep familiarity with the controlling processes and circumstances. Atmospheric hazard analysis must start during mine ventilation design. It is necessary to use physics-based operator (FBO) models to gain advanced insight into the Hazard System of the Mine (HSM) for hazard analysis as well as hazard-preventive ventilation design and operation. ML is helpful for identifying the numerical coefficients of FBO models to represent HSM.

A new approach is developed to identify FBO models for HSM from monitored data for atmospheric conditions from operating mine for 327 days under normal operating conditions, inspired by a previous study (Danko, 2006) for the subject ML for model identification, called the NTCF model technique. The nature of the methane mass influx due to pressure-driven, diffusive Darcy's flow with time was studied using the NTCF model technique in a previous progress report, and published already from the current work (Danko, 2022). The monitored parameters in the current study were air flow rate in the face drift (Qa), incoming methane (CH_4) gas concentration at the MG (c_{MG}), exiting methane concentration at the TG (c_{TG}), and barometric pressure Pb , all sampled at 5-minute time intervals.

For physics-based, methane flux calculation as the root cause for atmospheric methane concentration, the following matrix equation is used:

$$Q_M = M_M \cdot A \cdot (P_{st} - \hat{P}) + Q_0, \quad (5)$$

where Q_M , M_M , A , $P_{st} - P$, and Q_0 are respectively the methane mass flux Q -vector, [kg/s]; the admittance matrix of the methane transport's operator, [kg/s/m²/Pa]; the surface area, [m²]; the pressure driving force Q -vector [Pa] from monitored barometric pressure data at the working face; and the initial methane emission mass flux Q -vector, Q_0 [kg/s], assumed to be kept at zero. The $M_M \cdot A$ term may be considered a calibrated, but an *a priori* PBO in (5). As shown in (5), the root cause methane influx, Q_M , may be affected by the barometric pressure change in the ventilating air, \hat{P} .

Barometric pressure change may be caused by, for example, (1) fan malfunction, (2) roof collapse, (3) ventilation system control change such as fan speed change or air door closing or opening, (4) material haulage, (5) water or gas inburst from the strata, (5) sudden air temperature change, or (6) outside barometric pressure change such as during a passing weather front or storm. The identification of a PBO for the M_M operator and its application is reported in detail in Task 6 b.

Task 6. Fast-Forward Predictor for Hazard Evaluation.

Fast-forward model predictor tests continued between years 2 and 4 based on both DMVM and AI models, described in detail in interim reports and summarized in Appendix 1.

a. Fast-forward DMVM tests with the DQO model.

The DQO model was applied for demonstrating a mine safety application. DQO models were identified from in situ AMS data obtained for 327 days under normal operating conditions for all relevant

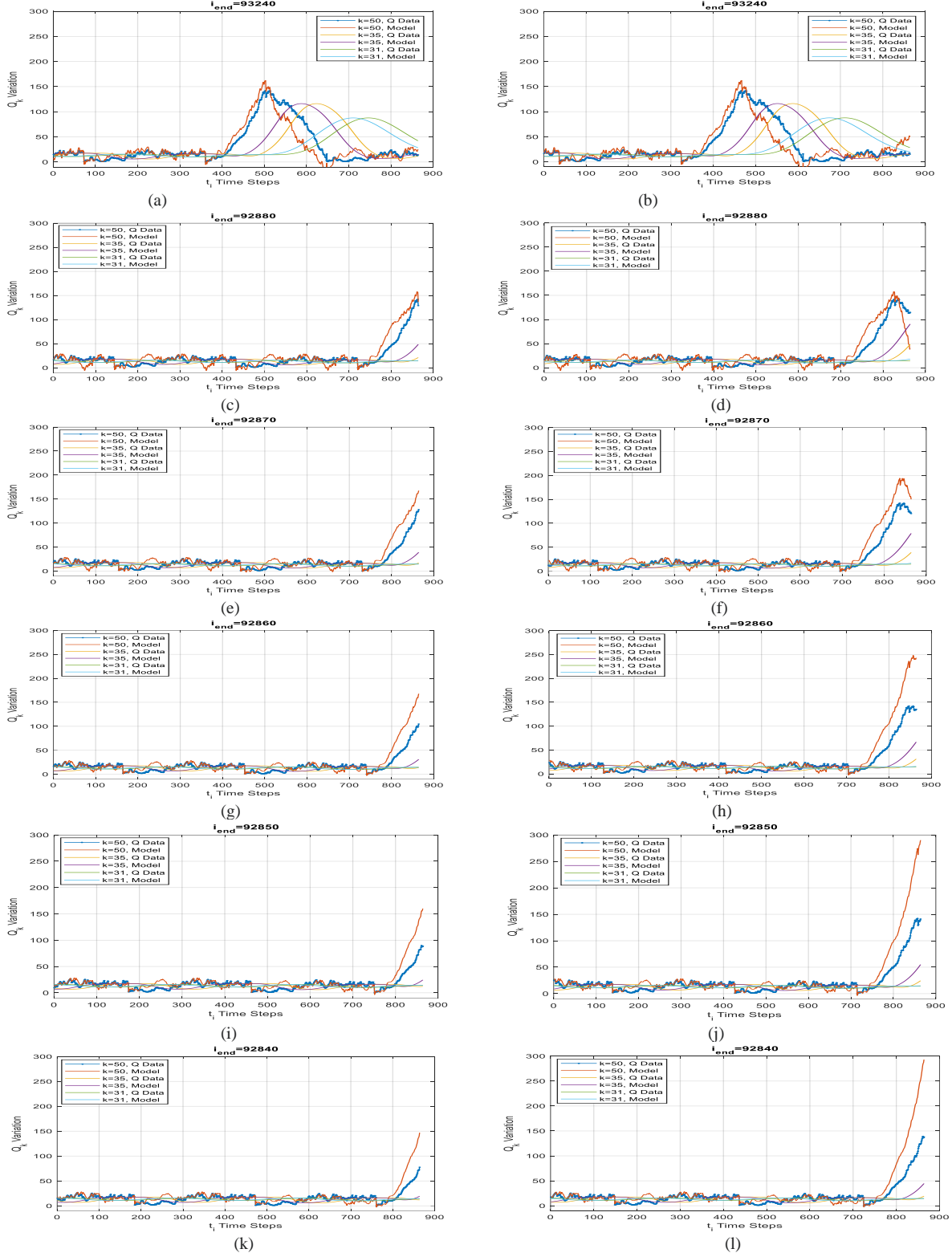
atmospheric parameters to mine safety. These parameters were barometric pressure (P_b), air flow rate in the face drift (Q_a), incoming methane gas concentration at the main gate (MG), exiting methane concentration at the tail gate (TG), and methane source (Q_m) seepage into the mine workings from the face cut and the ground during mining.

As no hazardous signal was ever detected during the 327 days of recorded mining operations, a synthetic data modification was introduced in day 300 by an added methane source (Q_{ms}) over the longwall face cut as a root cause for hazard. The goal was to forecast the effect of a triangular-shaped (linear increase, followed by a linear decline) Q_{ms} gas inburst over a 6-hour time period by the DQO model for preventive intervention before condition for a fatal explosive condition may happen.

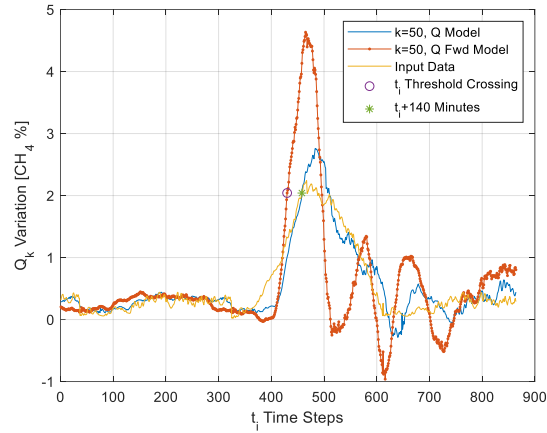
The DQO methane source model identification fitting and DQO forward prediction described in Task 5 was tested over a sliding 3-day time period with changing $t(i_{end})$ end date. The results are shown in Figures 19 a, c, e, g, i, k (left sub-plots) for DQO model fit for part of a disturbed day; and in Figures 19 b, d, f, h, j, l (right sub-plots) for 36-step forward prediction from the DQO model. The real-time component of the \mathbf{Q} vector ($k=50$) results from DQO model fitting (left sub-plots) show a good trend recognition with somewhat early (leading) methane inflow recognition relative to the measured and processed \mathbf{Q} data from AMS signal. The leading nature of the DQO model comes from differentiation originated from a single time step difference in the self-correlation fitting concept. The forward-prediction results by 36 time steps (right subplots) show an even stronger leading model trend versus \mathbf{Q} -processed AMS data, useful for forward prediction of the methane concentration from the future methane source, using the DMVM for concentration prediction without the need for further forwarding in time.

The methane concentration forward prediction curves are depicted in Figure 20, back calculated by the DMVM from the forward predicted methane source model of DQO. The results include three curves: a direct, methane concentration DQO model fit and prediction (with 1 forward time step for model identification) over the disturbed day (\mathbf{Q} Model for $k=50$); a 36-step methane (CH_4) concentration forward prediction for a disturbed day (\mathbf{Q} Fwd Model for $k=50$) from the combined use of DQO and DMVM models; and the AMS input methane concentration data processed into a \mathbf{Q} vector form. Two values are also shown: a 2% methane concentration threshold crossing point on the \mathbf{Q} forward model curve (with 'o') ; and the 2% methane concentration threshold crossing point on the input data curve (with '*'). An actual 28-step (140 minutes) forward prediction gain is seen from the DQO forward prediction model, a success for the test exercise to EWS application.

Further test results are shown in Figures 21 a - g for various shapes and durations of synthetic input methane inburst source variations with time. The goal of these illustration examples is to show the sensitivity of matching the DQO model output with measured input data; and evaluate the actual forward-prediction time gain from the model simulation result of the \mathbf{Q} _Fwd model by comparison with the measured input data. The number of forward time steps is reduced to $z=10$ as a lowered expectation. The time-gain between the \mathbf{Q} _Fwd output and the measured data is always evaluated at the 2% CH_4 concentration level in Figures 21 a - g. As shown, as the rise of the methane inburst becomes faster, the time gain is gradually reduced. For a step change rise, there can be no time gain, an understandable conclusion as there is no time left for the model to respond before the threshold crossing is completed, shown in Figure 21 g.



Figures 19 a-l. Records of DQO methane source model identification fit and DQO forward prediction over a sliding 3-day time period with changing $t(i_{\text{end}})$ end date; (a,c,e,g,i,k): DQO model fit for part of a disturbed day; (b,d,f,h,j,l): 36-step forward prediction from the DQO model.



Figures 20. DQO model fit and a 36-step methane (CH_4) concentration forward prediction for a disturbed day; an actual 28-step (140 minutes) forward prediction gain is shown from the DQO forward prediction model.

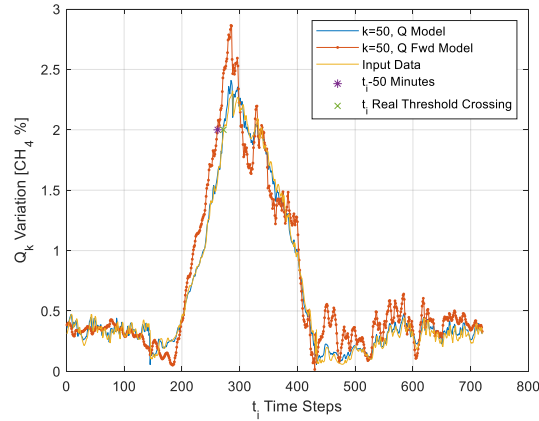


Figure 21 a. Arch-shaped CH_4 inburst input in 24 hrs (the expected forward prediction time of 10 forward steps agrees with the simulated outcome result).

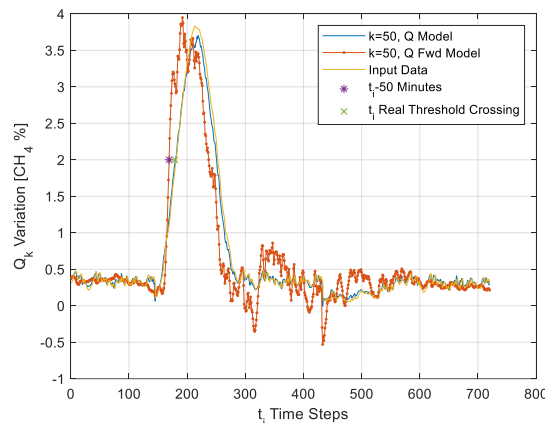


Figure 21 b. Sinusoidal-shaped CH_4 inburst input in 24 hrs (the expected forward prediction time of 10 forward steps agrees with the simulated outcome result).

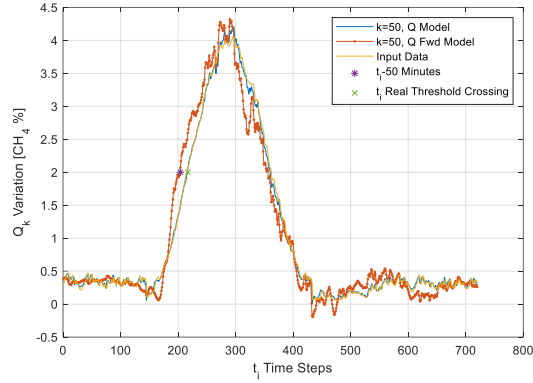


Figure 21 c. Cosine-shaped CH₄ inburst input in 24 hrs (the expected forward prediction time of 10 forward steps agrees with the simulated outcome result).

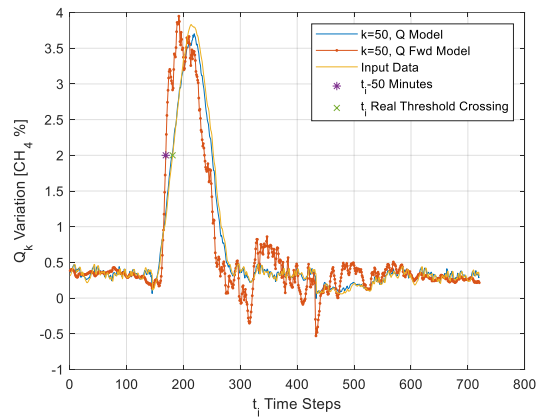


Figure 21 d. Cosine-shaped CH₄ inburst input in 12 hrs (the expected forward prediction time of 10 forward steps agrees with the simulated outcome result).

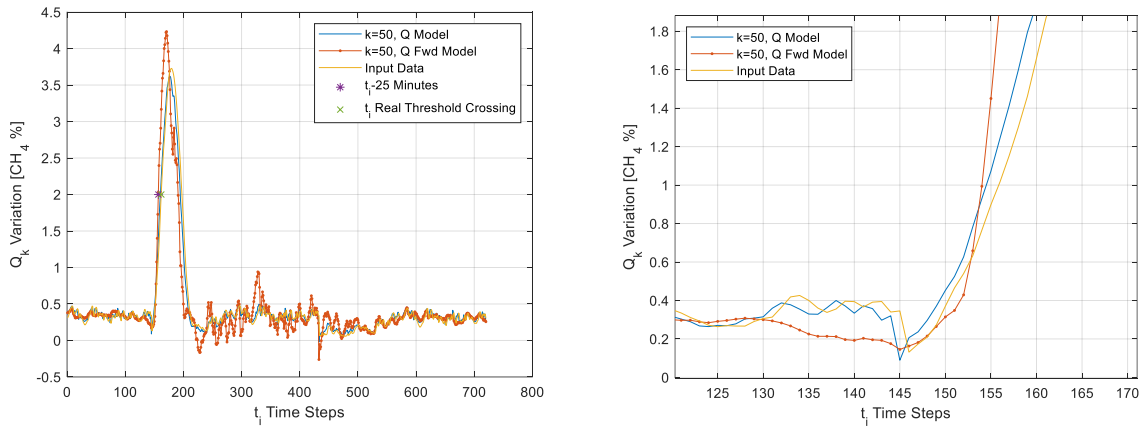


Figure 21 e. Left: cosine-shaped CH₄ inburst input in 6 hrs (the expected forward prediction time of 10 forward steps cannot be fulfilled); Right: zoom-in figure of the graph, showing that the Q model lags behind the measured data, whereas the Q_Fpd model starts up fast and soon leads the other curves.

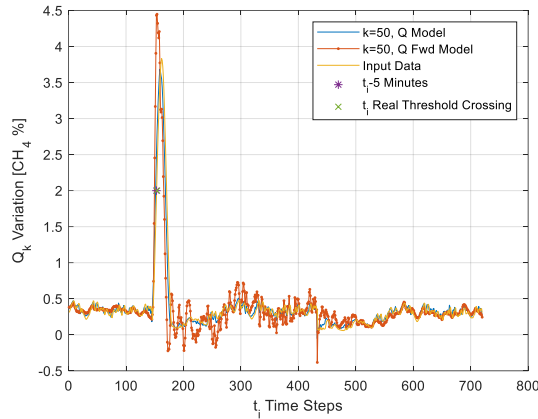


Figure 21 f. Cosine-shaped CH₄ inburst input in 6 hrs (the expected forward prediction time of 10 forward steps cannot be fulfilled).

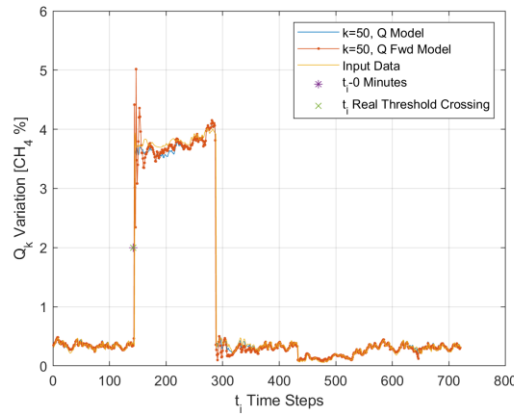


Figure 21 g. Square-Shaped CH₄ inburst input lasting for 12 hrs (the expected forward prediction time of 10 forward steps cannot be fulfilled).

b. FDO and DMVM tests for fast-forward predictions of possible methane incidents.

The work continued in years 3 and 4 with developments and tests, published, and described in detail in interim reports and summarized in Appendix 1.

The fastest forward prediction of a hazardous event may be achieved by running the pre-determined PBO model of the subject event. Once the first sign of the event's trigger signal is recognized, the PBO can instantly inform the mine's manager about the evolution of a hazardous episode moving toward an accident. A universal, ML method is developed and tested for determining PBO models of hazard-causing mining processes from AMS data during normal mining operations. Such PBO models can then be used for fast forward predicting hazardous outcomes if extreme triggering events are detected.

Such extreme triggering signals may come straight from AMS data or other sensors, e.g., from outside weather forecast. Triggering signals may be further enhanced by fast-forward DQO time-accelerator model elements. This way, the PBO models do not have to provide further time acceleration.

A PBO processor was developed for obtaining a Functionalized Data Operator (FDO) model that was trained to approximate past and present, input-output data relations. The kernel function of the FDO model is the fundamental solution of a general PBO methane transport model. The FDO model was designed to predict future output features for deviated input vectors from any expected, feared of conceivable, future

input for early-warning hazard evaluation. The linearized FDO was designed to provide fast analytical, input-output solution in matrix equation form, described in detail in an open-access journal publication (Danko, 2022). Numerical verification exercises were completed for FDO model identification and hazard evaluation focused on methane inflow into the working face from the face and the gob in an underground coal mine.

First, the M_M matrix of an FDO model was identified (further details are in Danko, 2022) from matching monitored methane mass influx data, \hat{Q}_M , (as a root cause) into the longwall section between the MG and TG locations, as a function of the barometric pressure variation, \hat{P} :

$$\hat{Q}_M = M_M \cdot A \cdot (\hat{P}_{\min} - \hat{P}), \quad (6)$$

where \hat{P}_{\min} was selected as the minimum of the barometric pressure value for an initial time period at the first location of the longwall face cut. The FDO models were identified to match the monitored methane influx data from (6) in the following matrix-vector form:

$$\begin{bmatrix} Q_{M1} \\ Q_{M2} \\ \vdots \\ Q_{MN} \end{bmatrix} = M_M \begin{bmatrix} (P_{\min} - P_1) \\ (P_{\min} - P_2) \\ \vdots \\ (P_{\min} - P_N) \end{bmatrix}, \quad (7)$$

where the Q -vector elements $1 \dots N$ in (7) covered a moving time window selected to be 10, 15, or 35 days. The selection of the model size for matching the observed, short-term variations with time in the measured data of methane inflow followed the parsimony concept of Occam's Razor (Danko, 2022).

Reducing size N of the M_M matrix operator in an AI-based model relates to its complexity for grasping the underlying processes which control the outputs for given inputs. The concept of Occam's Razor is the principle of parsimony with the minimization of N , a virtue worth considering for improving the model's quality and providing solvability.

Reducing the complexity of the model without reducing N for gaining better predicting power also calls for Occam's Razor. The model's size, N , affects the grasp of the history effects and the delay mechanism of substance transport between cause and response. Once the FDO model is identified, simplification may be done by eliminating the history effect not from the model, but from the input data, equating the past variations with the most recent, measured value. This means a step-change input (as if the same input has persisted from time zero) for finding the response function from the FDO model at every fine time step. Such a model simplification may be executed by replacing M with a diagonal matrix, M_D as follows:

$$M_D(j, j) = \begin{cases} \sum_{i=1}^j M_M(j, i), & j \in [1, N], \quad i \in [1, j]. \\ 0 & i \neq j \end{cases} \quad (8)$$

Each M_M matrix of the FDO models was determined over 90,000 steps, moving forward in 5-minute intervals (covering over 300 days of operation) continuously while training each FDO model for 10, 15 and 35 days of sliding window time periods.

Second, a DMVM equation was used to calculate the methane concentration at each time step at the TG location as follows:

$$\hat{c}^{TG} = \hat{c}^{MG} + \hat{Q}_M / \hat{Q}a, \quad (9)$$

where $\hat{Q}a$, \hat{c}^{TG} , and \hat{c}^{MG} are the monitored air flow rate, [kg/s]; monitored concentration at the tail gate [kg/kg]; and monitored concentration at the main gate [kg/kg].

Comparisons were made between the modeled and monitored methane concentrations at the TG location, after all repeatedly modeled and sampled variables were transformed into Q-vector forms in size of $N \times nT$.

For real-time data analysis and forecasting, the concept of Occam's Razor was used, reducing the size of the matrix operator and the \mathbf{Q} -vectors, N , as well as reverting to a simplified model, converting the full matrix to diagonal elements. Experimentation was necessary to find the best combination of N , nT (history time span, that is, the sliding time window with N divisions), and k (number of repetitions of the the \mathbf{Q} -vectors at Δt successions).

Synthetic, extreme barometric pressure variation was created from the monitored \hat{P} data steam by superimposing two, negative, absolute barometric pressure spikes starting at the 40000 and 60000 time steps, shown in Figure 22 as positive difference steps of $\hat{P}_{\min} - \hat{P}$ over all time steps. The absolute pressure spikes include 10 steps of linear descent by 5000 [Pa], 10 steps of the negative plateau, and 10 steps of linear ascent to the undisturbed value, all shown as positive pressure difference changes.

ORP1: Perturbed input pressure prediction using the first Occam's Razor's FDO model.

The first FDO model used a reduced-size selection of $N = 10$, $nT = 10$ days (2880 time steps); $k=10$ days (2880 time steps) for \mathbf{Q} -vectors processing; and FDO model identification for each 5-minute, real time instant over the allowable time period that stretches from day 10 (step 2880) to day (327-11) (approx. step 91000). Each of the approx. 87000 model was identified for analyzing of the sub-system around the subject time instant or forecasting its behavior in the immediate future before the next data and sub-model became available.

The model prediction results are shown in Figure 23. The modeled methane flux variations over 300 days are depicted (on the left) by three curves: (1) $\hat{Q}_{10}(10, t_i)$, measured, unperturbed; (2) $Q_{10}(10, t_i)$, perturbed, predicted by the full \mathbf{Q} model; and (3) $Q_{10}(10, t_i)$, from the \mathbf{Q}_D model, (left). Figure 24 (on the right) shows enlargement for four days of curves (1)-(3).

The model prediction result for the percentage of methane concentration using the subject FDO with the hypothetical, synthetic, perturbed barometric pressure input is shown in Figure 24. The modeled methane concentration variations over 300 days are depicted (on the left) by three curves: (1) $\hat{Q}_{10}(10, t_i)$, measured, unperturbed; (2) $Q_{10}(10, t_i)$, perturbed, predicted by the full \mathbf{Q} model; and (3) $Q_{10}(10, t_i)$, from the \mathbf{Q}_D model, (left). Figure 24 (on the right) shows enlargement for four days of curves (1)-(3).

ORP2: Perturbed input pressure prediction using the second Occam's Razor's FDO model.

The model prediction result for methane flux using the subject FDO with the hypothetical, synthetic, perturbed barometric pressure input is shown in Figure 25. The modeled methane flux variations over 300 days are depicted (on the left) by three curves: (1) $\hat{Q}_{15}(15, t_i)$, measured, unperturbed; (2) $Q_{15}(15, t_i)$, perturbed, predicted by the full \mathbf{Q} model; and (3) $Q_{15}(15, t_i)$, from the \mathbf{Q}_D model, (left). Figure 25 (on the right) shows enlargement for four days of curves (1)-(3).

The model prediction result for the percentage of methane concentration using the subject FDO with the hypothetical, synthetic, perturbed barometric pressure input is shown in Figure 26. The modeled methane concentration variations over 300 days are depicted (on the left) by three curves: (1) $\hat{Q}_{15}(15, t_i)$,

measured, unperturbed; (2) $Q_{15}(15, t_i)$, perturbed, predicted by the full Q model; and (3) $Q_{15}(15, t_i)$, from the Q_D model, (left). Figure 26 (on the right) shows enlargement for four days of curves (1)-(3).

ORP3: Perturbed input pressure prediction using the third, averaged-type Occam's Razor's FDO model with the 10×10 model size.

The model prediction result for methane flux using the subject, averaged FDO with the hypothetical, synthetic, perturbed barometric pressure input is shown in Figure 27. The modeled methane flux variations over 300 days are depicted (on the left) by three curves: (1) $\hat{Q}_{10}(10, t_i)$, measured, unperturbed; (2) $Q_{10}(10, t_i)$, perturbed, predicted by the averaged Q model; and (3) $Q_{10}(10, t_i)$, from the Q_D model, (left). Figure 27 (on the right) shows enlargement for four days of curves (1)-(3).

The model prediction result for the percentage of methane concentration using the subject, averaged FDO with the hypothetical, synthetic, perturbed barometric pressure input is shown in Figure 28. The modeled methane concentration variations over 300 days are depicted (on the left) by three curves: (1) $\hat{Q}_{10}(10, t_i)$, measured, unperturbed; (2) $Q_{10}(10, t_i)$, perturbed, predicted by the averaged Q model; and (3) $Q_{10}(10, t_i)$, from the Q_D model, (left). Figure 28 (on the right) shows enlargement for four days of curves (1)-(3).

ORP4: Perturbed input pressure prediction using the third, averaged-type Occam's Razor's FDO model with the 15×15 model size.

The model prediction result for methane flux using the subject, averaged FDO with the hypothetical, synthetic, perturbed barometric pressure input is shown in Figure 29. The modeled methane flux variations over 300 days are depicted (on the left) by three curves: (1) $\hat{Q}_{15}(15, t_i)$, measured, unperturbed; (2) $Q_{15}(15, t_i)$, perturbed, predicted by the averaged Q model; and (3) $Q_{15}(15, t_i)$, from the Q_D model, (left). Figure 29 (on the right) shows enlargement for four days of curves (1)-(3).

The model prediction result for the percentage of methane concentration using the subject, averaged FDO with the hypothetical, synthetic, perturbed barometric pressure input is shown in Figure 30. The modeled methane concentration variations over 300 days are depicted (on the left) by three curves: (1) $\hat{Q}_{15}(15, t_i)$, measured, unperturbed; (2) $Q_{15}(15, t_i)$, perturbed, predicted by the averaged Q model; and (3) $Q_{15}(15, t_i)$, from the Q_D model, (left). Figure 30 (on the right) shows enlargement for four days of curves (1)-(3).

ORP5: Perturbed input pressure prediction using the full, averaged FDO model with 35×35 model size

The model prediction result for methane flux using the subject, averaged FDO, M_{MA} , with the hypothetical, synthetic, perturbed barometric pressure input is shown in Figure 31. The modeled methane flux variations over 300 days are depicted (on the left) by three curves: (1) $\hat{Q}_{35}(35, t_i)$, measured, unperturbed; (2) $Q_{35}(35, t_i)$, perturbed, predicted by the averaged Q model; and (3) $Q_{35}(35, t_i)$, from the Q_D model, (left). Figure 31 (on the right) shows enlargement for four days of curves (1)-(3).

The model prediction result for the percentage of methane concentration using the subject, averaged FDO with the hypothetical, synthetic, perturbed barometric pressure input is shown in Figure 32. The modeled methane concentration variations over 300 days are depicted (on the left) by three curves: (1) $\hat{Q}_{35}(35, t_i)$, measured, unperturbed; (2) $Q_{35}(35, t_i)$, perturbed, predicted by the averaged Q model; and (3) $Q_{35}(35, t_i)$, from the Q_D model, (left). Figure 32 (on the right) shows enlargement for four days of curves (1)-(3).

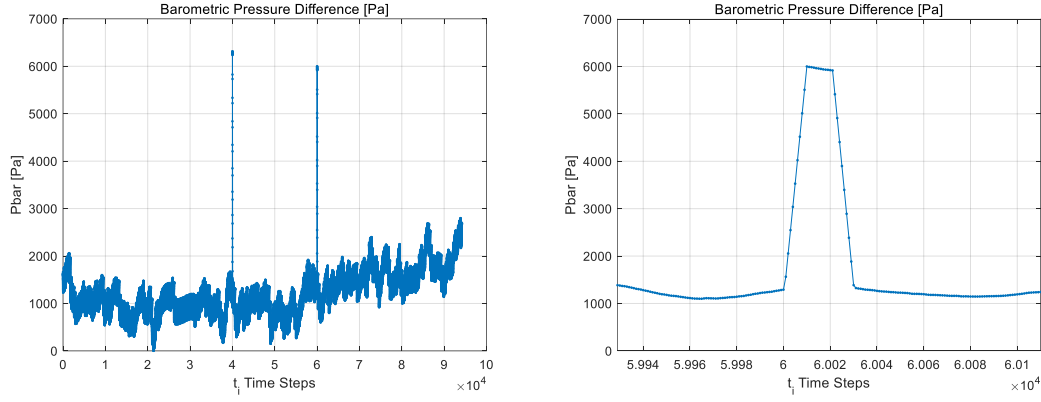


Figure 22. Assumed barometric pressure variation with two synthetic, extreme, barometric pressure spikes at 40000 and 60000 time steps (left); and enlargement of one spike (right).

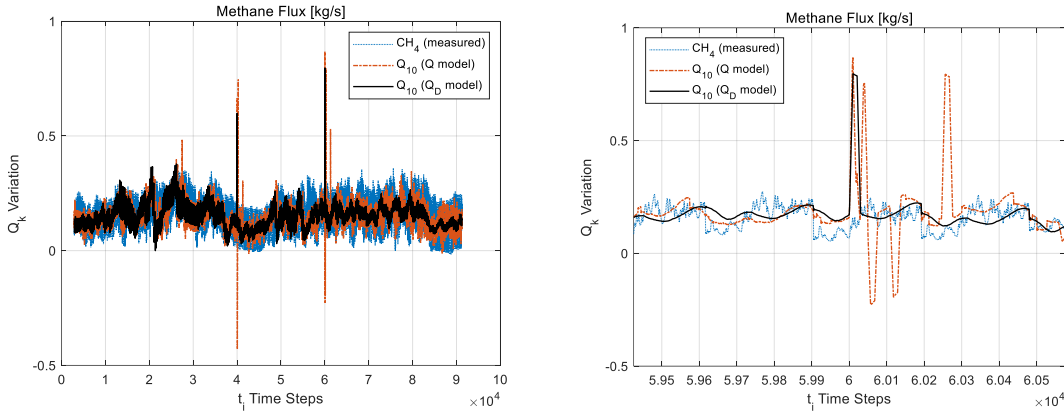


Figure 23. (ORP1) Modeled methane flux over 300 days: $\hat{Q}_{10}(10, t_i)$, measured, unperturbed; $Q_{10}(10, t_i)$, perturbed, predicted Q model; and $Q_{15}(10, t_i)$, Q_D model, (left); enlargement for four days (right).

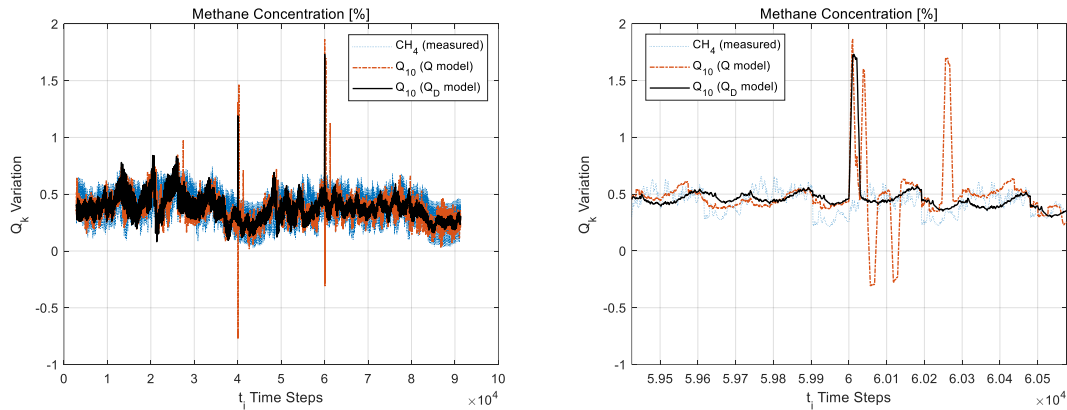


Figure 24. (ORP1) Modeled methane concentration over 300 days: $\hat{Q}_{10}(10, t_i)$, measured, unperturbed; $Q_{10}(10, t_i)$, perturbed, predicted Q model; and $Q_{10}(10, t_i)$, Q_D model, (left); enlargement for four days (right).

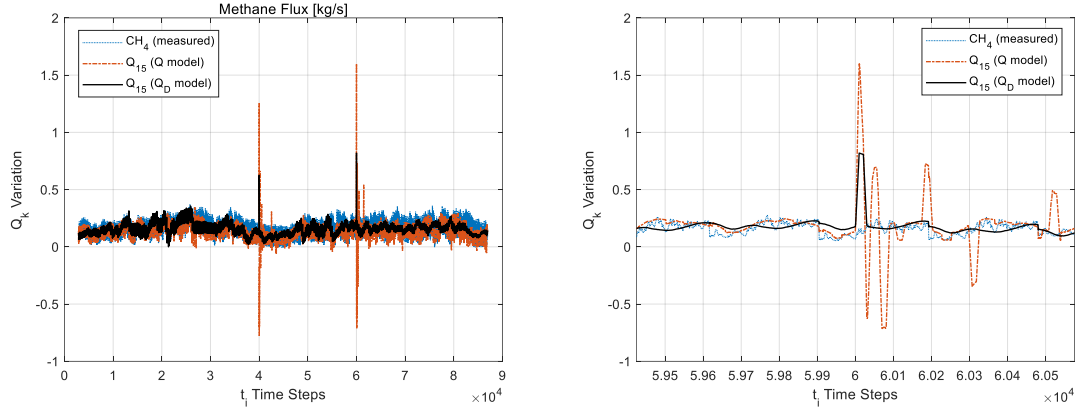


Figure 25 (ORP2) Modeled methane flux over 300 days: $\hat{Q}_{15}(15, t_i)$, measured, unperturbed; $Q_{15}(15, t_i)$, perturbed, predicted Q model; and $Q_{15}(15, t_i)$, Q_D model, (left); enlargement for four days (right).

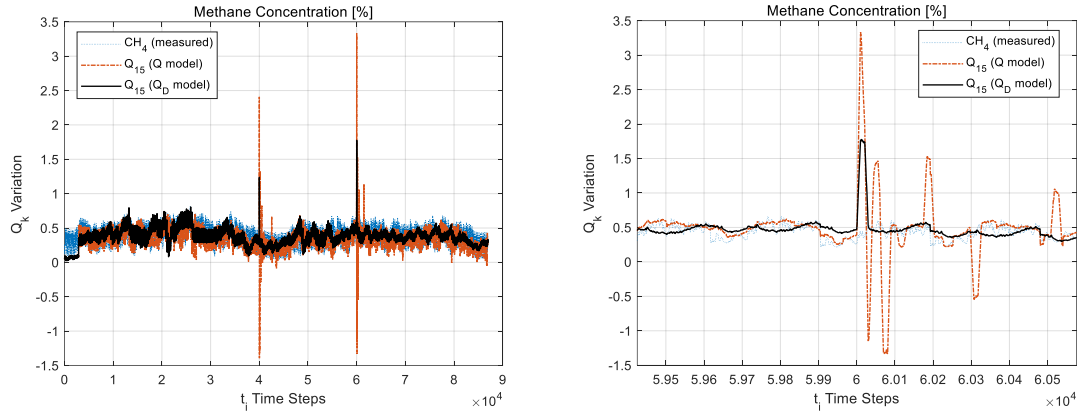


Figure 26. (ORP2) Modeled methane concentration variations over 300 days: $\hat{Q}_{15}(15, t_i)$, measured, unperturbed; $Q_{15}(15, t_i)$, perturbed, full Q model; and $Q_{15}(15, t_i)$, Q_D model, (left); enlargement for four days (right).

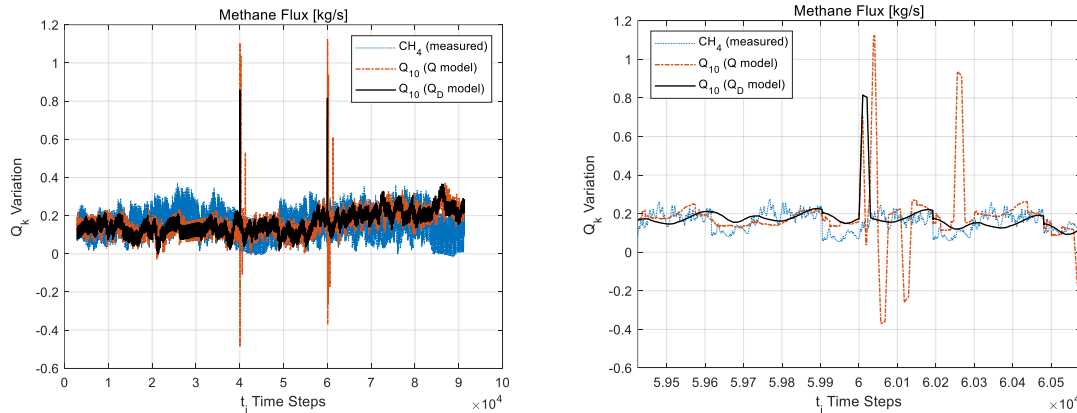


Figure 27. (ORP3) Modeled methane flux variations over 300 days: $\hat{Q}_{10}(10, t_i)$, measured, unperturbed; $Q_{10}(10, t_i)$, perturbed, predicted by the averaged Q model; and $Q_{10}(10, t_i)$, from the Q_D model, (left); enlargement for four days (right).

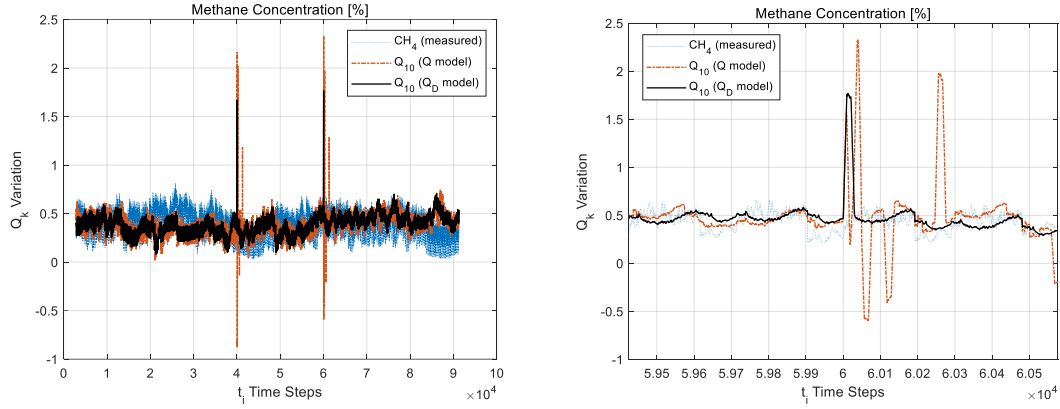


Figure 28. (ORP3) Modeled methane concentration over 300 days: $\hat{Q}_{10}(10, t_i)$, measured, unperturbed; $Q_{10}(10, t_i)$, perturbed, averaged Q model; and $Q_{10}(10, t_i)$, Q_D model, (left); enlargement for four days (right).

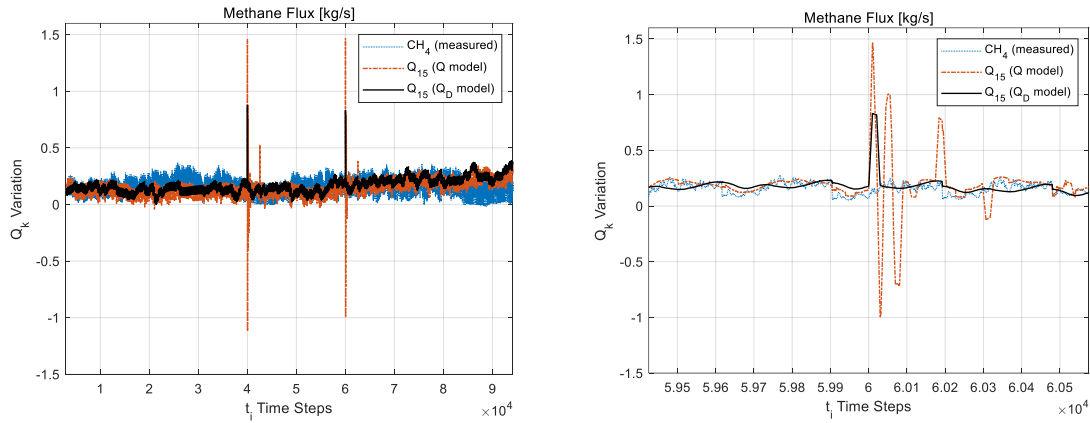


Figure 29. (ORP4) Modeled methane flux over 300 days: $\hat{Q}_{15}(15, t_i)$, measured, unperturbed; $Q_{15}(15, t_i)$, perturbed, averaged Q model; and $Q_{15}(15, t_i)$, Q_D model, (left); enlargement for four days (right).

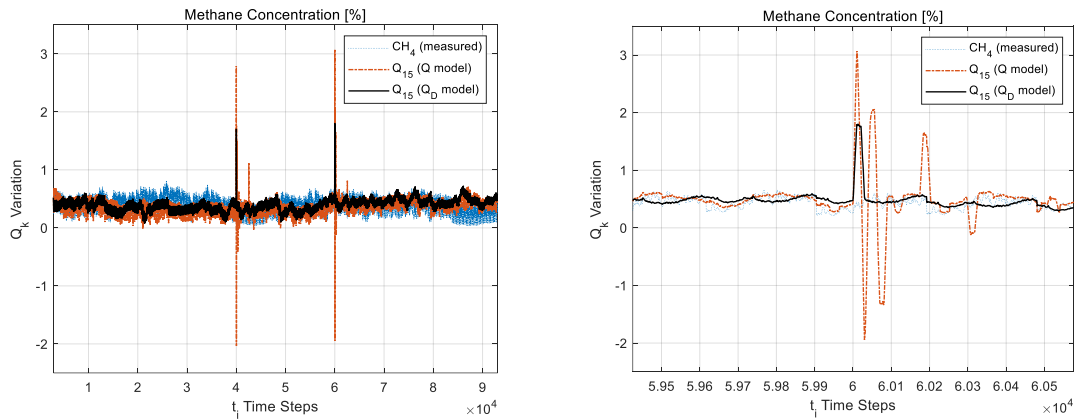


Figure 30. (ORP4) Modeled methane concentration over 300 days: $\hat{Q}_{15}(15, t_i)$, measured, unperturbed; $Q_{15}(15, t_i)$, perturbed, averaged Q model; and $Q_{15}(15, t_i)$, Q_D model, (left); enlargement for four days (right).

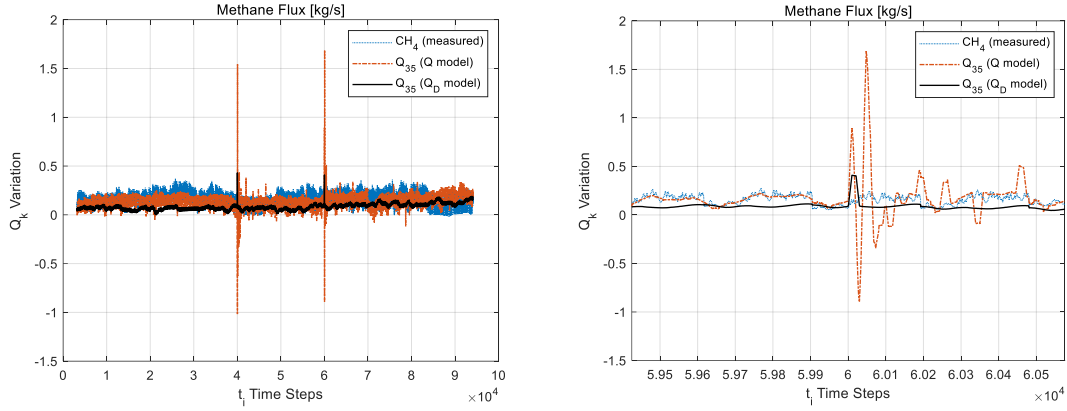


Figure 31. (ORP5) Modeled methane flux variations over 300 days: $\hat{Q}_{35}(35, t_i)$, measured, unperturbed; $Q_{35}(35, t_i)$, perturbed, predicted by the averaged Q model; and $Q_{35}(35, t_i)$, from the Q_D model, (left); enlargement for four days (right).

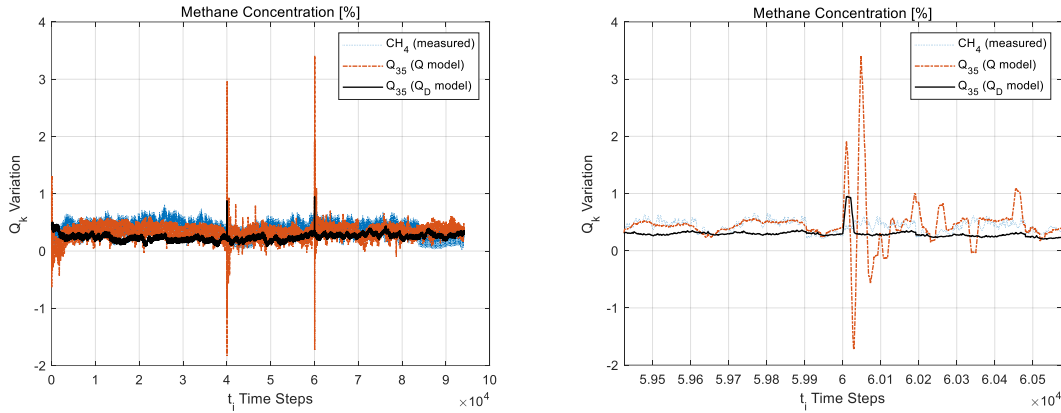


Figure 32. (ORP5) Modeled methane concentration variations over 300 days: $\hat{Q}_{35}(35, t_i)$, measured, unperturbed; $Q_{35}(35, t_i)$, perturbed, predicted by the averaged Q model; and $Q_{35}(35, t_i)$, from the Q_D model, (left); enlargement for four days (right).

Task 7. EWS Hazard Evaluator.

Hazard evaluation software tests continued between years 2 and 4 based on both DMVM and AI models as reported in the interim reports with results and conclusions.

- The presented numerical test with emulated, synthetic malfunctions represent disturbances typical from fan failure; roof collapse; gas outburst; gob outgassing; and mine fire. Hazard evaluation regarding gob outgassing was executed with a native Ventsim solver at five selected time periods in Year 2, reported in an interim report, listed in Appendix 1).
- Safety test buttons trial the EWS. All emulated, synthetic signals were prepared to be sent into the EWS Hazard Evaluator, emulating also the “safety test” button activation. Future applications of EWS with Safety, Health and Efficiency Output Generator outputs will require integration into the Ventsim Control software.

Task 8. Design EWS Safety, Health and Efficiency Output Generator.

EWS output generator for hazard condition in Task 8 was planned in year 2 and exercised in manual tests. Automation is straightforward, based on tested EWS safety threshold crossing. Future applications

of EWS with Safety, Health and Efficiency Output Generator outputs will require integration into the Ventsim Control software.

- a. Safety hazard notification to mine management. Planned in the first and refined in the second year.
- b. Safety factors to support OVC or VOD decisions for economic benefits. Referred to automation in existing Ventsim Control functions with support from EWS signals.

Task 9. Tests of EWS Outputs for Safety, Health and Efficiency.

- a. Safety hazard notification tests from synthetic data. Tests were discussed with Ventsim Designers for the project period, waiting for full integration in the Ventsim Control host processor.

Task 10. Reporting

Three Annual and four Semi-Annual Reports, including two Milestone reports in the year 2 and year 3 Annual Reports were submitted.

4.0 Research Findings and Accomplishments

Conclusions of the DMVM in the EWS

A Computational Energy Dynamics model is developed for fast mine ventilation, heat, and contaminant transport simulations with the ability to handle the dynamics referred to the “flywheel effects.” The innovative NTFC component used in the MF-based DMVM model is in close physical relationship to the AI-based FDO model that can be identified from AMS data, a new discovery from the EWS project.

Interpretation and conclusions of the DQO model for analysis and forecast.

A quantum-vector -based DQO model was developed for fast processing of the mine’s AMS data model analysis and forecast in time. The DQO model has surpassed any other ML methods in the numerical tests for time series AMS data processing and forward predictions. Therefore, the DQO has an excellent potential to be a core element in EWS software applications in the future.

The successful tests of the DQO model in the EWS for up to 1 hour forward-step forecast for temperature forecast and 3 hours for methane forecast makes the method appealing, especially in comparison to published results for NN models with poorer forward prediction performance for only one forward time step.

Both the DQO model identification and its forward prediction results show excellent stability. The error ranges shown in Figures 12 a, b, 14 a, b, 16 a, b, and 18 a, b prove that the predicted results are well bounded and can be reliably used for hazard warning, considering that a reduced EWS trigger level to half of the accepted safety value can easily compensate even for a maximum of 100% prediction error.

Interpretation and conclusions of the FDO model for analysis

A PDO-based FDO model is developed for deep-understanding a mine’s health and safety characteristics that determine the mine’s responses to unforeseen atmospheric, natural, or operational disturbances. The FDO model shows excellent potential to be a core element in EWS software applications in the future.

Application of the FDO model with strongly perturbed, suddenly increased barometric pressure input, significantly different in shape and nature from the monitored data used in FDO model identification raises

the risk of errors due to the potential presence of false correlation in the input and output data streams. Such false correlation may be suspected due to the common influence of mining activities and operations at the longwall face upon both monitored and recorded input pressure and output methane concentration data. Lacking proof to exclude it, a hypothesis must be made about the lack of such false correlation for accepting the results presented hereby for FDO model analysis forecasting.

As depicted in Figures 24 through 33, the model predictions for methane liberation due to pressure-depression pulses generally agree, all showing responses in methane flux pulses within a -1.5 to 1.5 [kg/s] range for the 300 m face drift. The larger the model size from $N = 10$ to 35, the higher the methane flux peaks in both the negative and the positive direction.

The extreme, negative values from a linear model must be interpreted as a physically invalid extrapolation, well outside the small, all-positive validity range, that is used in model identification. Only the positive methane flux, entering the air flow is physically plausible. Methane mass flux may pulsate within a positive domain up and down used as the input data for model identification. Methane flow direction from the air flow into the strata is inconceivable, as methane mixes with air rapidly and only a low-concentration mixture (but not pure methane) may be driven back to the porous and fractured strata under forcing driving pressure.

However, the tendency to block methane inflow right after the start of the Q-vector of the negative pressure pulse reveals useful methane transport information about the linearized system. It would be counterproductive to consider forcefully eliminating the unwanted negatives from the results. The beginning part of the Q-vector refers to the oldest data in the sliding window, varying from about 5.5 days ($N = 10$) to 70 days ($N = 35$). The beginning part of the $\hat{P}_{max} - \hat{P}$ pressure Q-vector may be initiating methane blockage from a farther distance in the methane-bearing strata and starting a “peristaltic wave” of methane flux into the airway, culminating in a series of positive and negative pulses toward the latest time, showing dynamic fluctuations and definite time delays in Figures 22-32.

The diagonal simplification of the FDO model replaces M with a diagonal matrix, M_D , shown in (8). The physical meaning of diagonalization is an assumed history variation change in the driving force’s Q-vector (that is, in \hat{P}), forcing to replace the real, variable history (used during model identification) into an abstracted, step change variation in \hat{P} , constant from the beginning to the most recent value. The step change solution eliminates the delayed, “flywheel” effects in the prediction for methane flux with time in the simplified, diagonal model solution.

It is interesting to see that all diagonal, M_D model solutions (marked as Q_D curves), show acceptable (albeit somewhat simplified) match to the measured, unperturbed data, but robust, single, positive methane flux as well as methane concentration responses to pulse-type perturbations. Note that M_D inherits all information carried in the full M matrix of the FDO model, and it integrates, rather than forcefully eliminates unwanted response components.

It is convenient to use the modeled pulses for the methane flux rates and the methane concentrations from the M_D models for their apparent stability marked as Q_D curves in Figures 22-32. The small size, sliding window, full model with $N = 10$ appears to be satisfactory for the response analysis to barometric pressure depression pulses. Each model is trained over a 10-day sliding time window, with past data sampled every 5 minutes for 2880 readings for processing the input Q vectors. Each model is evaluated within 10^{-3} sec on a regular laptop computer. Each model is updated every 5 minutes, allowing the EWS software to adjust to operational changes, and evaluate model consistence relative to previous models.

5.0 Publication Record and Dissemination Efforts

- Danko, G., (2022). “Functionalized Data Operator Model for System Analysis and Forecasting.” *Applied Mathematics*, 13(12), <https://www.scirp.org/journal/am>, doi: [10.4236/am.2022.1312062](https://doi.org/10.4236/am.2022.1312062), pp. 988-1021.
- Dias, T. A., (2021) “Methane concentration forward prediction using machine learning from measurements in underground mines,” M.S. Thesis, University of Nevada, Reno.
- Dias, T., Belle, B., and Danko, G., (2021), “Methane Concentration forward prediction using machine learning from measurements in underground mines,” The Australian Institute of Mining and Metallurgy Publication Series No 7/2021, Proceedings, AusIMM Conference, 2021, pp. 4-23, ISBN 978-1-922395-02-3.
- Danko, G., (2021). “Quantum Operator Model for Data Analysis and Forecast.” *Applied Mathematics*, 12, <https://www.scirp.org/journal/am>, ISSN Online: 2152-7393 ISSN Print: 2152-7385, pp. 963-992.
- Danko, G., Bahrami, D., & Stuart, C., (2020). “Applications and verification of a computational energy dynamics model for mine climate simulations.” *International Journal of Mining Science and Technology*, Volume 30, Issue 4, July 2020, pp. 483-493.
- Danko, G. (2019). “Computational Energy Dynamics Model for Mine Climate Simulations,” Proceedings, 17th North American Mine Ventilation Symposium, Montreal, Canada, pp. 1-12.
- Danko, G., (2019), “Safety, Health and Cost Benefit Optimization with Accident Intervention Assistance,” SME presentation, February 25, 2019.
- Danko, G., (2019), “Computational Energy Dynamics Models for Mine Climate Simulations,” SME presentation, February 25, 2019.

In-person and online seminar presentations during Covid 19 lockdown in Australia:

Seven presentations were given as follows reporting the results of the PI’s work in Australia during a 4-month Fulbright Research program related to the Alpha Foundation project:

- (1) “Safety, Health and Cost Benefit Optimization with Early Warning System Assistance,” April 5, 2020, Brisbane, Howden Office. (Audience: research partners from Howden and a local mining company).
- (2) “Technology Elements for Future Mines Design,” April 5, 2020, Brisbane, Howden Office. (Audience: research partners from Howden and a local mining company).
- (3) “Enabling Technology Elements for Future Mines Design,” May 20, 2020, (Zoom Presentation) University of Adelaide. (Audience: Professors and research students; Organizer host: Prof. Michael E. Goodsite, A/Prof. Chaoshui Xu).
- (4) “Technology Elements in Future Mines Design,” May 22, 2020, (Microsoft Team Presentation), UNSW, University of Sydney. (Audience: Professors and research students. Organizer host: Prof. Bruce Hebblewhite, A., Prof. Saiied Aminossadati).
- (5) “Technology Elements in Future Mines Design,” May 22, 2020, (WebEx Presentation), WASM, Curtin University, Perth. (Audience: Professors and research students. Host: Prof. Vishnu Pareek).

- (6) “Technology Elements in Future Mines Design,” May 29, 2020, (Zoom Presentation), University of Queensland, Distinguished Lecture Series. (Audience: Professors and research students. Host: A. Prof. Saeed Aminossadati)
- (7) “Safety, Health and Cost Benefit Optimization with Accident Intervention Assistance,” June 2, 2020, (WebEx Presentation), WASM, Curtin University, Perth. (Audience: Professors and research students. Host: Prof. Vishnu Pareek).

Reports

2019 Mid-Year Report
2019 Annual Report
2020 Mid-Year Report
2020 Annual Report
2021 Mid-Year Report
2021 Annual Report
2022 Mid-Year Report

6.0 Conclusions and Impact Assessment:

The practical output of the 4-year research project is the development of the system frame of the EWS software complete with innovative AMS data management processes, prototype-tested DMVM model components and ML-AI processor elements. The mathematical foundations of the innovative processes are all tested and published in refereed, leading technical journals in the field.

The challenges problems addressed in the research proposal to the Alpha Foundation were solved with innovative engineering methods.

We maintained a working partnership with the dedicated developers of the Ventsim Visual software at Ventsim Howden, Brisbane, Australia. They are interested in further pursuing marketing the EWS for word-wide mining applications for the safety and health of the workers in the mines and for the safety of the mining operations.

We trust that the methods and software tools developed in the funded project for the EWS are the most advanced in the field, worthy for the endeavor for world-wide marketing for practical applications.

7.0 Recommendations for Future Work:

- The AI models of DQO and FDO, the NTCF for the DMVM model, and the EWS framework and data handling structure will need to be incorporated in Ventsim Design and Ventsim Control. The issue of using a different source code, Matlab for the DMVM model in MF and EWS elements and Ventsim’s C++ and .net dll environment will remain to be solved beyond the current project’s timeline.
- Since computational speed and accuracy is less important due to the reduction in the role of DMVM in fast-speed data evaluation using new and innovative AI model elements, the EWS baseline software may rely solely on Ventsim’s current solver engine without incorporating the faster and more accurate MF engine.

- However, for accurate simulator models for mine ventilation, heat and contaminant transport, and especially, with mine fire, a true, thermodynamic-based transport model solver will be needed, currently available only in MF. A fully integrated linkage between Ventsim and MF, therefore, is timely, and highly recommended.
- It will be necessary to recheck the EWS software functions against real-time data streams after the DQO, FDO and NTCF model parts are integrated into Ventsim's current data handling system. The onsite training of the PI and working sessions in December, 2022 in Brisbane, Australia was helpful in deciding future cooperation in this area and in EWS marketing to the mining industry.
- It may also be necessary to work together with the Vensim Control developers in Canada for any software transfer to Ventsim Howden as they are also involved in AMS data handling.
- For real-time signal evaluation tests, recorded ('conserved'), as well as live data can be likewise used as an emulator frame controller that can pass the data at the sampling speed from the database to the EWS for processing evaluation as a remote, cloud-computing EWS testing application.
- Further mine tests and data are being sought for progressing EWS toward mining applications, especially for a metal mine in Nevada as an NDA has already been signed between UNR and NGM for cooperation in EWS tests.

8.0 References:

- Danko, G., (2022). "Functionalized Data Operator Model for System Analysis and Forecasting." *Applied Mathematics*, 13(12), <https://www.scirp.org/journal/am>, doi: [10.4236/am.2022.1312062](https://doi.org/10.4236/am.2022.1312062), pp. 988-1021.
- Dias, T. A., (2021) "Methane concentration forward prediction using machine learning from measurements in underground mines," M.S. Thesis, University of Nevada, Reno.
- Dias, T., Belle, B., and Danko, G., (2021), "Methane Concentration forward prediction using machine learning from measurements in underground mines," The Australian Institute of Mining and Metallurgy Publication Series No 7/2021, Proceedings, AusIMM Conference, 2021, pp. 4-23, ISBN 978-1-922395-02-3.
- Danko, G., (2021). "Quantum Operator Model for Data Analysis and Forecast." *Applied Mathematics*, 12, <https://www.scirp.org/journal/am>, ISSN Online: 2152-7393 ISSN Print: 2152-7385, pp. 963-992.
- Danko, G., Bahrami, D., & Stuart, C., (2020). "Applications and verification of a computational energy dynamics model for mine climate simulations." *International Journal of Mining Science and Technology*, Volume 30, Issue 4, July 2020, pp. 483-493.
- Danko, G., (2006). "Functional or Operator Representation of Numerical Heat and Mass Transport Models," *ASME J. of Heat Transfer* (IF 0.776), Vol. 128, pp. 162-175.

9.0 Appendices:

Appendix 1. Description of the activities and results in each tasks in each year

A1.1.1. Discussion of the results of the work in year 1

Detailed documentation of the work is provided in the Appendices of the 1st Semi-Annual and 1st Annual reports.

A1.1.1. EWS model setup tests with Ventsim and MF-DMVM comparison

a. Ventilation flow and pressure models

- A conceptual, simplified, deep, and hot, vertical intake shaft, a straight, long horizontal drift, and an exhaust shaft were modeled under forced ventilation by a main fan both in Ventsim and MF-DMVM.
- The simulation results showed very good agreement between the two models both in the flow rates and air pressures.

a. Dynamic thermal model

- It was not possible to get daily flywheel results from Ventsim. The results of a daily flywheel simulation from Multiflux was demonstrated without difficulty.
- The annual temperature variations for one year after a five-year pre-ventilation period was tested for comparison between Ventsim and MF-DMVM for six selected points along the network model. The general agreement was reasonable, but a gradual deterioration was observed with increasing distance, showing a 10% to 80% difference in dry bulb temperature between Ventsim and MF-DMVM simulations, depending on time over the year.
- In conclusion, the EWS design using the MF-DMVM was found to be the prudent way to proceed.

A1.1.2. EWS model and mine AMS data comparison

- Monitored AMS mine data was also analyzed for gaining familiarity from 11 sensor stations from a partner metal mine in Nevada for (1) air flow rate, (2) temperature, (3) Carbon monoxide (CO) concentration and (4) Oxygen (O₂) concentration for two 14-day time periods in March and April, 2019.
- Data were evaluated for inspection and signal processing exercises. The raw data sampled every minute, showed various imperfections including outliers, unrealistic values and missing readings. The signature of temporal changes appeared to be induced by regularly variable mining activities.
- Overall, manual observation of the data with respect to time could not notice correlations for gaining good understanding of the temporal data variations.
- Ventsim's native solver agreed in monthly-averaged temperatures on sensor 1 and 2 locations closely with the measured, mean temperatures, but on statistical sense the Ventsim results were found somewhat off the statistical range, and lower than the measured real temperatures, showing the need for model calibration.

A1.2. Discussion of the results of the work in year 2

Detailed documentation of the work is provided in the Appendices of the 2nd Semi-Annual and 2nd Annual reports.

A1.2.1. Tests of EWS using AMS data with Ventsim and MF-DMVM models

a. Gob model setup tests

- In situ mine data were obtained from a large operating coal mine in Australia for the EWS tests. A complete AMS dataset was received from the operating mine to support our studies, aiming at matching, and evaluating measured data, including model self-calibration and root-cause analysis, with our dynamic simulation models.
- The data set included a full, 3,687 x 310 m longwall panel for its 327 days of operation. The EWS simulation model tests started with the evaluation of the variations of the daily-average gas concentrations against mine data from 16 monitoring locations in the longwall panel over the entire recorded time period. AMS data of air flow, pressure, temperature, O₂, CO, CO₂ and CH₄ gas components were included at 16 moving AMS stations during coal extraction over the 327 days.
- The first goal was to set up the simulation model of the gob, the connecting airways, and the coal strata in both Ventsim and MF-DMVM. A gob dynamic network model was first set up in Ventsim, capable of simulating and following the atmospheric conditions in an entire longwall panel with a moving face cut drift in each day, linked to a “schedule table” for modifying the geometrical and flow resistance parameters of the network model. Substantial in-kind support was received from the Howden-Ventsim development team in linking the gob model setup for the EWS task to the Ventsim Visual and also Ventsim LiveView a version. (Note: LiveView has since been replaced by the Ventsim Control version).
- A gob outgassing model was added to the DMVM as a transient model component. The liberation of Methane from the coalbed during drift development and longwall shearing operations was modeled using the methods in transport phenomena in porous media, starting with Darcy’s law that expresses the flow of a fluid driven by the pressure gradient.
- The time-dependent mass transport model for gas flow in porous media was developed as a “Numerical Transport Code Functionalization “ (NTCF) model resulting in a matrix-vector equation with an NTCF matrix operator depending only on the geometry and geophysical properties of the coal seam and the gob. The model is described in detail in the 2nd Semi-Annual Report in 2020.

b. AMS data matching with DMVM by input parameter adjustment

- The second goal was to check if the DMVM model could be kept calibrated against monitored data during operations. It was found that the simplified DMVM model prediction for Methane concentration at the shearer location moving over the 3687 m length in 327 days could match the average trends of measured Methane concentration variations with time and location reasonably well by the adjustment of the input property values of the geophysical input data of the gob.
- However, the un-calibrated model cannot show enough variation of the daily concentration oscillations. These monitored concentration oscillations around the smooth trends from the simplified DMVM model indicate local inhomogeneities in gas release rates possibly due to fractures and/or high-permeability stress zones encountered during production.
- Methane source variations with location and time are expected to be the fact of life during mining in a longwall panel. The model must be matched to the changing situation that is random in nature and cannot be learned from past encounters captured by the AMS data. The only “known unknown” is that running into high-permeability locations such as joints, cleats, bedding plates and stress-relaxation locations will happen; and various amounts of methane and other gas species will be released.

- In order to perform an effective self-calibration of the dynamic methane transport model, the process must recognize and further anticipate changes in the model parameters from the measured concentrations in comparison to the causal, predictive DMVM model.

c. AMS data matching with DMVM by self-calibration with root-cause analysis

- Self-calibration helps close the difference between model prediction and measured concentration variations with location and time in the longwall panel example. Even a simple method of backcalculating a “dynamic Methane influx difference” as a “self-calibration Methane flux (SCMF)” from the difference between the AMS and DMVM concentrations, and adding this SCMF term to the simulated Methane influx could be quite effective in finding a reasonable agreement between model prediction and monitored results.
- The application of ML and AI with NN was initiated, discussed in Appendix 4 in the Semi-Annual report of the 2nd year. Using the AMS signal trends of the longwall operation of the mine, AMS data matching and future events predictions were tested. It was concluded that while good data matching was reached during the training time period, good forward prediction ahead of even just a few days of time cannot be achieved.
- It was concluded that training the NN model for a 50-day previous time interval, a future sample of event may not be self-similar to the prior series of events. Therefore, learning from the past series cannot give valid value of a single future event but only for its self-similar statistics.
- The question was raised if the NN model’s best use is not the prediction of the future value but the changing direction of the signal whether it is likely increasing or decreasing one time-step ahead. A future value can be predicted with the use of the observed value of the previous day’s average observation, $C(t)$, and the first derivative of the daily trend, $dC(t)/dt$. If the $dC(t)/dt$ parameter can be predicted from the NN model, then keeping it constant for predicting the next-day average value can be calculated as $C(t+1)=C(t)+dC(t)/dt$.
- A plan was made for NN model tests for forward prediction of the first derivative of the signal change in future exercises.
- It was anticipated that the model calibration would have to be in two different time scales, one using daily-average concentration data and one applying the minute time scale data for rapid evaluation of concentration peaks during the day. Figure 2 in Appendix 1 shows the logic flow chart of the proposed DMVM model matching scheme using the dual time scales.

A1.2.2. Further tests of EWS using AMS data with Ventsim and MF-DMVM models

a. Data abstraction for synthetic data based on in situ mine data.

Lacking a full, minute-scale AMS data set from our partner mine, it was necessary to use minute-scale AMS data sets for the dual time scale EWS tests in addition to the daily data of the coal mine used before. The real-time, daily averaged mine data was combined with the limited number of minute time scale data from AMS with randomly combined, abstracted, synthetic variations for the amplitudes of the minute scale concentrations around the daily-averaged data in lieu of real mine data. Such input data abstraction was necessary to proceed with the EWS tests in data management and the fast forward prediction algorithms to simulate normal operations (with amplitudes not exceeding explosion limit) as well as in checking worrisome situations. This is consistent with our original, proposed method of testing out-of-the ordinary situations with synthetic data for higher-than acceptable peaks to trigger early warning. Once the EWS prototype software is tested against the mine-originated, but

synthetically abstracted data, it will be straightforward to switch to real, fine-scale mine data in future applications.

- Barometric pressure (BP), air flow rate (Qm) and the concentrations of O₂, CO, CO₂, and CH₄ were selected for gas concentration studies from the AMS sensors. Eight sensor stations were selected for the EWS software tests, and their daily average as well as minute scale variations were examined for acceptability, detailed in the Annual Report of the 2nd year. The data referred to various stages and working configurations of the mining operation providing a good insight of the expected variations of the monitored parameters.
- The ranges of the average, minute-to minute variations (AMV) were quite high for the selected days, exceeding the 100% variation range relative to the daily-averaged readings over the 327 sampled days. It was found to be surprising, however, that the average, day-to-day variation (ADV) of the daily-averaged data was small, e.g., , 0.1%, 1.1%, 4.5%, 11.5%, 13.8%, 4.0%, 4.3% and 4.5% for the BP, Qm, and the six Methane concentration points. This was explained by the 1445 number of minute-averaged samples used for the calculation of each daily-averaged signal value by the data acquisition system at the mine.
- The relatively modest ADV values for the signals have a profound benefit for signal processing in the EWS. Accordingly, the fast-forward prediction of daily signal averages can be calculated from first-order extrapolations of the daily averaged signals for estimation of the data 1 day ahead of time. In short, the daily-averaged mine AMS data can be used as the self-similarity model of the mine for a 1-day forward prediction of all expected, averaged values. The question, however, remains open as to how the real-time signal evaluation at the minute-scale can be processed fast enough for hazard evaluation.

b. AMS signal evaluation results from DMVM

- The purpose of the EWS signal processing was to find out-of-the ordinary events from continuously evaluating the AMS signal trends. As the AMS of the mine employs concentration but not source sensors, the focus was on inverse identification of the species influxes as sources from concentrations. Causal relationships were established by transport model building from first principles; and statistical, signal processing, and by ML for AI model identifications such as NN.
- Transport model results for methane influx prediction at the longwall face drift were obtained calculated at fixed locations first and verified again that the fixed-position processing is not applicable to matching production concentration data which are related to an advancing longwall face cut and moving Methane source positions (for further detail please refer to Appendix 1 of the 2nd Annual Report).
- The results from DMVM for predicted sources showed that the NTCF model was missing much of "production" sources which could not be predicted as it was not known where they were coming from. This was one of the "known unknowns" in the mine which must be evaluated backward from the AMS data using daily average concentrations. The good feature is the low ADV, and good stability in the daily-averaged sources. The challenge is to process the EWS signal for accounting for the fast-changing sources which may vary widely.
- Methane concentration forward predictions by one day ahead were tested from days 1 through 327 at the MG and TG moving locations in the panel after self-calibration of the DMVM against AMS data. The resultant, daily averaged Methane concentrations at both the MG and TG locations

were very reasonably matched with the measured AMS signals in spite of a simplified, first-order extrapolation for a one-day forward prediction in the process.

- Forward-predicting future values of measured signals were further tested using the LSTM-type NN model described in Appendices 2 and 3 of the 2nd Annual Report.
- An integral analysis of the time-variable, minute-scale mass influxes was carried out at the six selected positions for four selected days. It was found that the minute-averaged sources only modulate up and down the methane influxes around the daily average value. It was concluded that these integral properties robustly show whether at any minute there is a negative “deficit” or a positive “surplus” of Methane source relative to the already forward-predicted, daily averages. Since hazard is related to increased concentrations over the predicted averages, only the time periods with positive, “surplus” sections should be of concerns for hazardous conditions. The continuous, integral evaluation of the instantaneous Methane source variation with time may be used as a robust element of a potential, future hazard evaluation.
- In addition to the integral analysis, it is important to continuously evaluate (1) the statistical homogeneity and (2) self-similarity of the seemingly stochastic, minute-averaged variations of Methane sources. Continuous, real-time checking of properties of (1) and (2) are needed to maintain “trust” that the daily-average values of the Methane influx over the integrated strata volumes and time each day in the mine will not change much and will agree with the first-order forward predictions from the one-day step ahead forecast.
- The periodograms of the minute-averaged Methane production sources were tested for the six selected locations and four sampled days. It was found that all valid signals were similar in characteristics, revealing a typical, uniform, statistical distribution of variation frequencies; whereas all appearing very different from a normal distribution that would show a horizontal shape. The data obtained from the sensors on January 13 do not follow the same trend, likely due to data acquisition system malfunction. This data, therefore, was discounted from the studies.
- A hypothesis was defined in the project, namely that as long as the periodograms characteristics follow a “machine learned” pattern, the typical, statistical homogeneity, property (1), and self-similarity, property (2) are both valid; and, therefore, the integral source variations may be reliably used for real-time hazard evaluation.

c. AMS signal evaluation results from ML with LSTM-type NN

- The LSTM tested in the project gave good predictions for data that had pattern, (sinusoidal function, for instance), where up to ten steps ahead could be predicted with a good degree of accuracy. However, when real data were used from AMS, the predictions were limited to a maximum of five steps ahead.
- The training time was also a concern for the LSTM type of NN, using the long-short term memory and the explosion gradient in the training process. Although it is a powerful version over the conventional NN and RNN methods the long training time and the short forward-predicting time period may not be practical in real-time EWS applications.

A1.3. Discussion of the results of the work in year 3

Detailed documentation of the work is provided in the Appendices of the 3rd Semi-Annual and 3rd Annual reports.

A1.3.1. Tests of AMS data processing and compression technique for the MF-DMVM model elements

The minute-average AMS data was processed into 5-minute average data for database size reduction as a “course” time division data for EWS model evaluations. It is expected that very rapid hazard events in the second time range will need no EWS model evaluation but rather an immediate emergency response from mine management.

- The 5-minute average data is fine enough for data variation representation and has the necessary information density of minute-sampled variables for the EWS simulations and evaluation. The size of data for each variable is 470,880 from 1440 minute-sampled daily values for each of the 327 days. Each active model network element will have to process this size of data.
- Transport processes involving storage of mass or thermal energy and having memory of history variations such as concentrations and temperatures must store past information up to the last time instant. Future predictions from present and past data must handle the large data flow.
- Methods were tested to compress the large amount of data without losing the essential information content in it in order to produce the fine time scale concentration and temperature variations while retaining the delayed transport features from long term history effects.

A1.3.2. Tests of MF-DMVM thermal and concentration model predictions using compressed AMS data
(Please refer to Appendix 3 of the 3rd Semi-Annual Report for further detail.)

- Numerical examples proved the applicability of the presented data compression technique. In the first thermal model application, on the one hand, only a few per cent differences were seen between the full and the approximate, compressed model results. Even the outliers were within the 10% difference range on the day-by-day basis, which was around the expected, targeted error in the EWS evaluation. On the other hand, the data compression and associated reduction in storage capacity as well as processing time was $94,176/50=29.22$ -fold, a major reduction, favoring the compressed, to the full model.
- In the coal mine examples with faster AMS data stream, the data compression and associated storage capacity as well as processing time was $1461/50=1883.5$ -fold, a more dramatic ratio.
- The examples involving large AMS data streams demonstrated the necessity to reduce the data sizes while maintaining the long-time history effects together with the fine details of the 5-minute-scale data variations.
- In view of the comparisons, common wisdom prefers faster model solution with a slightly lower accuracy than the other way around, especially considering that the DMVM model is meant to proceed with self-calibration at least each day-by-day time period.

A1.3.2. Tests of AMS signal pattern, trends, and root-cause processes

- The results showed that the LSTM and time-series techniques performed similarly, and both were sensitive to sliding window sizes and the number of forward-step predictions. The time series filter showed to be much faster than the LSTM model and presented a higher accuracy using the first order fitting and using the filtered data for training and predicting.
- The transport model-based root-cause Methane source evaluation provided a forward output with a more even relative error variation but slightly higher peak values than those obtained from the predictions using the time series filter. Nevertheless, the one-day forward prediction result for the root-cause CH₄ source as an “expected target limit” was the most useful parameter for EWS hazard evaluation for rating the risks due to the minute-scale variation of CH₄ influx variations during the previous day.
- The predictions were acceptable, but more tests were warranted to try to increase the accuracy of the predictions from the root-cause transport model.

A1.3.3. Model elements for AMS signal pattern, root-cause processes, and forward prediction evaluation

- As part of the DMVM and the AI model tools in EWS, a new Dynamic Quantum Operator (DQO) model was developed. The DQO model was tested to match dynamically monitored outside temperature, and Methane data for a coal mine. The DQO model was found advantageous regarding processing time, data compression, and modeling accuracy.
- A new paradigm was introduced for periodic, automatic model adjustment over long time intervals of regular operations to keep the DMVM model calibrated as mining conditions may vary with time. Since only self-calibration over long time periods (several hours or days) can be used for DMVM model adjustment in order to follow slow-changing and nonthreatening model conditions, a question was raised: if the DMVM model is needed for self-calibration against the AMS data why not only the AMS matching and already long-time-trained AI model (such as the DQO) is used instead for both model calibration and forward prediction?
- The combined use of the AI-based DQO model can simplify the EWS processor and gain precious time for early warning. Evaluating the root-cause source terms during calibration of the DMVM model or DQO model identification can eliminate the need for a fast-forward DMVM model prediction as the DQO model can forward predict the expected future source term from a recognized hazard directly.
- It is necessary to automatically recognize any short-time, fast, and potentially hazardous deviation between the regularly conditioned DMVM model results and the AMS data. The EWS warning evaluation must be triggered by an early detected, lowered threshold crossing of any designated gas concentration or temperature signal in the AMS data. The development and testing of such early-warning triggering processors is paramount to the success of the EWS software. Such a trigger processor using DQO was discovered and tested in two application examples in the project.
- As no hazardous event has taken place during the study time period, we used the same original AMS data in subsequent exercises with added, synthetic perturbations for emulating would-be scenarios for hazard evaluation and warning indication by EWS.
- In the original concept, it was necessary to identify the root cause of the fast and unusual signal deviation recognized by the evaluation for the fast-forward prediction of the future outcome of the disturbance. The original concept in the EWS used the DMVM model for root cause analysis as well as fast-forward prediction. The original concept requires (i) the evaluation of a variety of possible causes with a fast-running DMVM model to best match the deviated signal; and (ii) the accelerated-time simulation of the effect of the identified cause relative to the safety case, that is, the likely future occurrence of a threshold crossing of the flagged signal in real time. The two-step process of (i) and (ii) can be replaced with a single step process using the DQO model.
- The simplified concept uses the forward-predicted data from a DMVM-combined AI model instead of the DMVM forward prediction alone in EWS hazard evaluation. The new concept has three essential components: (a) the transport-process elements of the DMVM has already been gradually migrated into the AI model, providing guidance in causal relationships (for example, Methane mass influx as root cause is determined directly from AI model matching Methane concentrations while incorporating measured air flow rate in the evaluation); (b) AI model matching over long-time intervals already provide automatic self-calibration, eliminating the need for additional calibration; and (c) additional, root-cause evaluation and fast-forward simulation

becomes unnecessary as the primary, critical signal is forward predicted as an early-real-time forecast. The DMVM-based hazard evaluation will still be needed in the evaluation of safety and health conditions in the un-monitored areas of the mine.

- A hypothesis test about significant time gain is tested and affirmed for DQO model application in racing for preventive interventions to counter impending hazard events in methane concentration increase in the mine's atmospheric conditions. A time advantage of 150 minutes were gained by the early detection from the DQO model prediction, saved for preventive interventions to alleviate impending hazard conditions at mine's longwall face.
- Two different, forward-prediction algorithms were developed, based on the DQO model for mine safety and health applications: one used a multiple forward step DQO model training setup and a one-step forward prediction; the other a used single forward step DQO model training setup and a multi-step, cascaded forward prediction algorithm.

A1.3.3. NN and time series AI model elements for AMS signal pattern and forward prediction

- Tests of the LSTM predictions were found to be similar to those using the time series filter predictions. The LSTM tests showed that increasing the number of time steps in the training period did not increase the accuracy of the predictions.
- Increasing the number of forward time steps in future predictions rapidly increased the error between predictions and original target.
- The tests with the time series filter showed that it was much faster than the LSTM and it was easier to implement. The first order polynomial fitting gave the best results compared with the second order fitting and the LSTM model. Filtering the data made the predictions better for both LSTM and the time series filter.

A1.4. Discussion of the results of the work in year 4

A1.4.1 Paradigm change in AMS signal evaluation.

- The original concept of detecting a dangerous level of gas concentration before its real-time occurrence was based on three consecutive actions: (1) detecting a suspiciously rising concentration but still below the dangerous level (e.g., crossing 0.5% CH₄) at any concerned location; (2) finding the possible root-cause (e.g., CH₄ inburst at an upstream location, or air flow blockage due to roof collapse, etc.) with the DMVM or ML model for the rapid, but still low threshold crossing; and (3) finding the possible, continuing effects of the root cause at any concerned location at a future time with the fast-running DMVM or ML model; and (4) checking if a dangerous concentration level (e.g., 4% or higher) may be exceeded. Steps (1)-(3) require multiple, overlapped, repeated, simultaneous processes to be run parallel on the DMVM processor or the ML model checking also various hypotheses on the possible root causes. It has been demonstrated (e.g., in our July, 2021 report) that automatic model adjustment is necessary to keep the DMVM model calibrated as mining conditions vary with time without knowing how and why to place the root causes into the model as inputs. Predictions in Steps (2) and (3) are faster with ML models, however, their training time may be problematic, discussed in the July 2021 report.
- The new DQO model for forward prediction is faster and require less data to store. The forward-prediction result from the DQO model may allow to check expected outcomes (e.g., at each 5 minute time step) in future time (e.g., 25, 30, 50 minutes later time) at desired locations. Since the DQO model is trained to best match the monitored data of critical concentration at every time step

in past time, there is no need for additional DQO model calibration. Since the root cause is manifested in the monitored data, there is no need to “deep understanding” the root cause for finding its outcome other than matching the DQO model during its training continuously for every single time step.

- The AMS data evaluation needs storage, massive data processing, and machine learning. The DQO predictor uses compressed data and provides forward prediction for up to 20–30 time steps useful for fast signal and data processing. The most important, fast-response EWS functions by EWS data analysis may use the DQO processing in all monitored locations with only a few dynamic model-elements of the DMVM simulator in real-time applications.
- The much slower method of numerical modeling may only be needed for locations lacking atmospheric monitoring sensors (AMS), or for recognizing early on some slowly developing, but nevertheless disastrous events. These remaining EWS functions should still be done by high-precision DMVM in which the NTCF model method must be included.
- A linkage was developed between the DQO and the NTCF models for the critical branches where the NTCF model may be identified from the quantum vector data during the data processing automatically.
- It was discovered later in 2022 that better results may be obtained for identifying an NTCF-type operator model, a Functionalized Data Operator (FDO) (Danko, 2022) from the AMS data using sampled history input data instead of quantum vector data processed by weighted data integrals described and used in the DQO model.

A1.4.2. EWS evaluation tests

Tasks 1, 2, 3, 4, 5, 6, 7, 8, and 10 have been worked on during the reported time period, described and documented in detail, given in Appendices 1 and 2 of the 4th Semi-Annual report. Further detail in a new publication in 2022 is given in the referenced paper.

Task 1. Complete the EWS Framework.

AMS network and data mapping to the EWS. Compatibility in handling AMS data with the current Ventsim Control software was implemented in EWS design. The AMS data stream handling from 0.1-sec acquisition sampling to 5-minute average format was completed, coded, and tested. The AMS data from all sensors were processed from 0.1s sampling and stored in a new type of “Quantum Vector” (QV) format for Fast-Signal (FS) data, whereas one element of the FSQV was re-sampled at 5-min. intervals for storing in QV format for Slow-Signal (SS) data for further processing.

Task 2. The DMVM software in Multiflux.

Dynamic model elements and configurations for air flow, heat, moisture, and contaminant concentration. Compatibility in handling the dynamic CH₄ transport elements in DMVM with the current Ventsim Control software was implemented in EWS design, using the QV data format.

Task 3. The DMVM Model Calibrator.

DMVM model calibration processes. A unified Quantum Operator Predictor (QOP) and a Functionalized Data Operator (FDO) model were tested for identification of the NTCF (Numerical Transport Code Functional) model-element in the DMVM.

Automatic, self-calibration processes. Automatic extraction of NTCF-QOP and NTCF-FDO model-elements were tested from AMS mine data for pressure-driven CH₄ mass flow rate and concentration.

Task 4. Safety awareness processor.

AMS signal patterns recognition. Further tests were conducted using two types of QV data based signal pattern recognition methods: the ‘non-relativistic’ QOP model, described in the previous report, and the new, ‘relativistic’ NTCF-FDO model.

AMS trend analysis. Signal trends were studied for synthetically deviated AMS signals in barometric pressure and air flow rate input data, processed by the new, relativistic, NTCF-FDO method.

Task 5. The Root-Cause Evaluator in the EWS.

Signal processing methods for recognizing unusual patterns in the AMS signals. The NTCF-QOP and NTCF-FDO methods were tested for processing dangerous patterns for CH₄ spikes.

Root-Cause evaluation of model conditions and source terms in the DMVM. The NTCF-QOP and NTCF-FDO methods were tested for processing the CH₄ source term from AMS signal trends.

Task 6. Fast-Forward Predictor.

The fast-forward DMVM with NTCF components. The QOP and FDO were linked to the NTCF method in the reported period and the NTCF model element was incorporated in the DMVM model.

Fast-forward predictor tests. Further tests were made on the stability and applicability of the fast-forward prediction techniques regarding perturbed signal shapes.

Task 7. EWS Hazard Evaluator.

Gas liberation model tests. Strata and gob outgassing due to barometric pressure variations were tested with the NTCF-QOP and NTCF-FOD models.

Other proposed elements in this task are malfunctions in fan failure; roof collapse; gas outburst; and mine fire. A directed test was completed with air flow perturbation together with barometric pressure perturbation, representing either fan failure or roof collapse.

Task 8. Design EWS Safety, Health and Efficiency Output Generator.

Safety hazard notification to mine management. Conceptional design of the safety hazard output was completed in the reported period as these functions are proposed to be accessed directly from the real-time Ventsim Control host processor (see safety warning generation in the data processing scheme in.

Task 9. Tests of EWS Outputs for Safety, Health and Efficiency.

Safety hazard notification tests from synthetic data– tests were discussed with Ventsim Designers for the reported period, waiting for full integration in the Ventsim Control host processor.

Task 10. Reporting.

Progress Report. All reports completed.

Appendix 2. An early plan of DMVM model calibration in two different time scales.

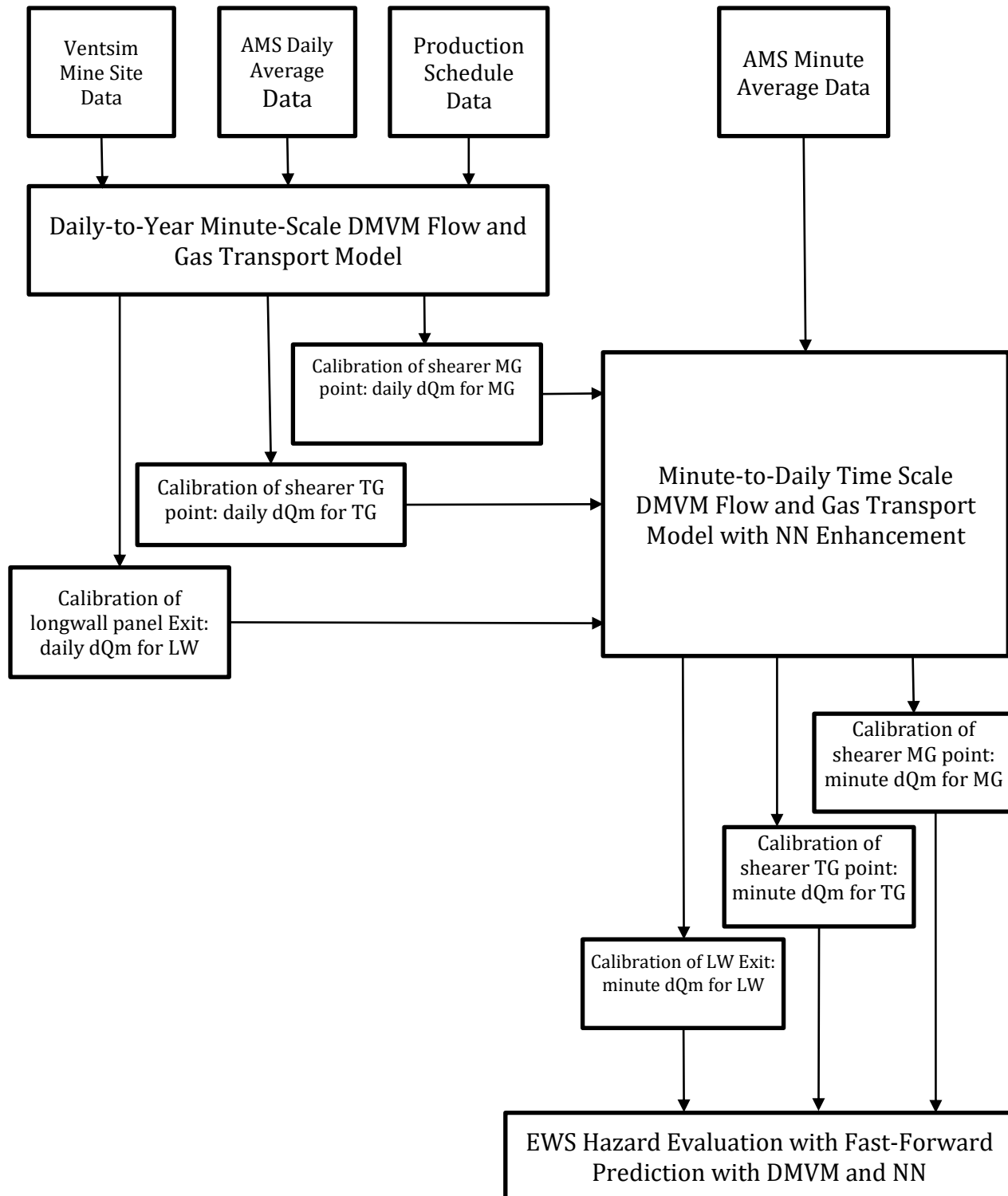


Figure A2.1. Logic flow chart of the DMVM model calibration against AMS data in two different time scales.

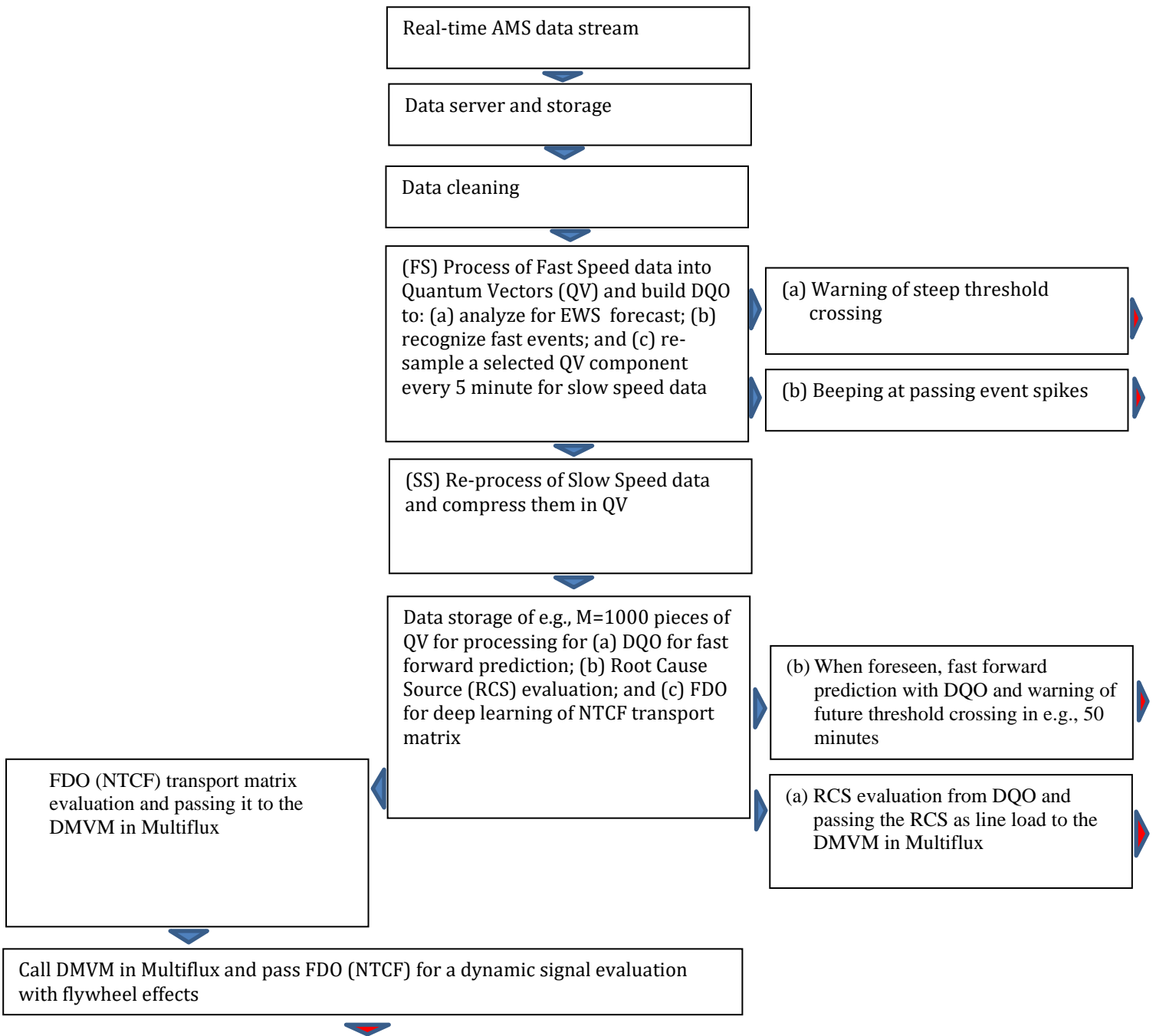


Figure A2.2. Logic flow chart of the EWS data handling in two different time scales.

Appendix 3: Improved MF coupled heat-flow solver.I

In this section, a challenging example has been set up to test the computational performance of the new and improved coupled heat-flow solver within the MF6 engine. Figure A3.1 shows the network layout prepared in Ventsim for a vertical multi-level network. The model includes a fixed flow fan, indicated in Figure A3.1, with 200 kg/s of mass airflow rate. Each branch also includes a 100 kW of sensible heat source. There are five surface nodes with three of them at the intake side.

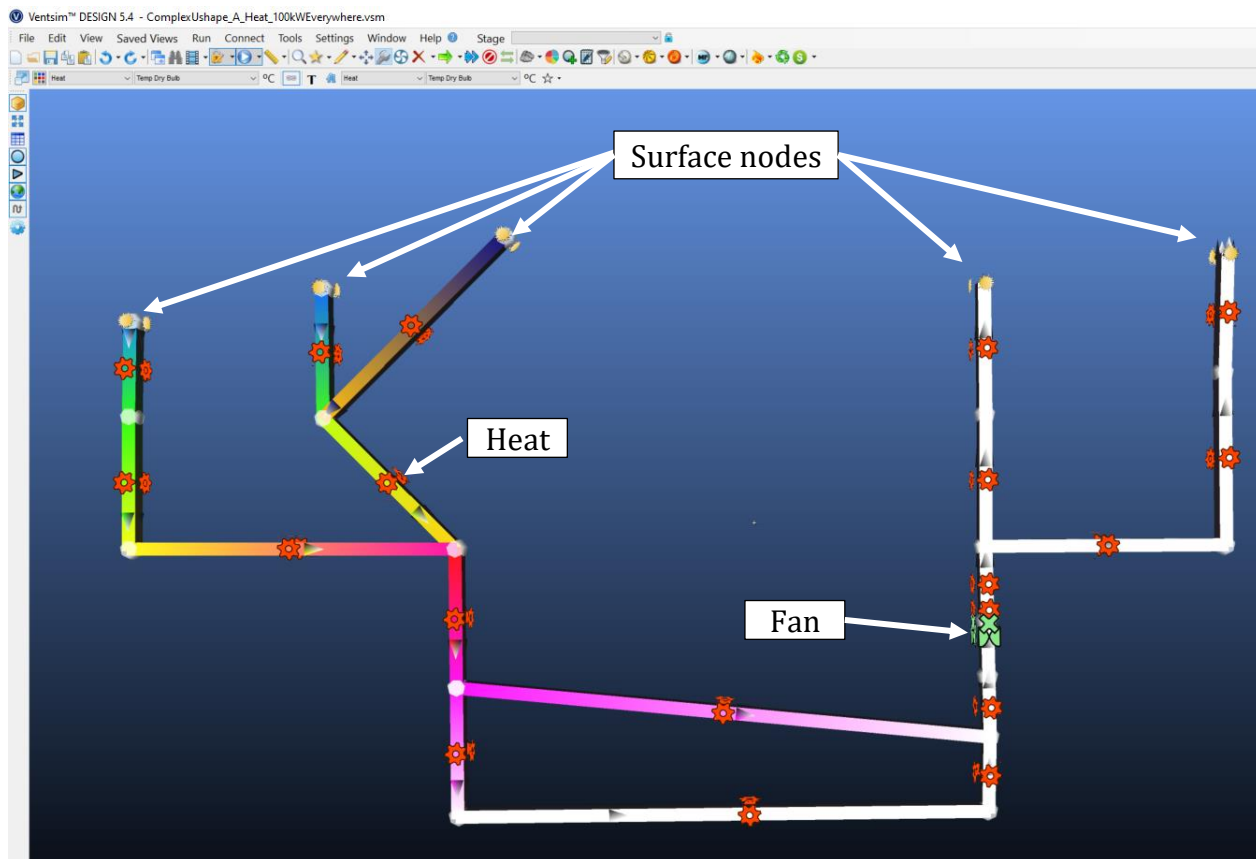


Figure A3.1. Ventilation model set up in Ventsim.

The model is transferred to MF6 solver to run the coupled heat-flow solver and plot additional information about the model setup. Figure A3.2 shows the branch ID along with the network layout with the flow direction. The 200 kg/s fixed flow fan is placed in branch 18. There are three intake boundary points on the left side of the network and 2 exhaust points on the right. Figure A3.3 shows the network layout with junction or Node IDs.

Figure A3.4 shows the flow solver convergence error down to $1e-9$ kg/s in 12 steps. A good convergence can also be achieved to below 0.01 kg/s in three steps. Figure A3.5 shows the convergence error curve for the coupled solution to within 0.001 °C in only 7 iterations.

Figure A3.6 shows the comparison of branch end pressures between Ventsim and Multiflux. The results are in excellent agreement with 40.3 Pa RMS error of the difference. Table A3.1 summarizes the comparison data for branch end temperatures.

Figure A3.7 compares the branch airflow rates between Ventsim and Multiflux. The results are in excellent agreement with 2.8 kg/s RMS error of the difference. Table A3.2 summarizes the comparison data for branch end temperatures.

The comparison of branch end temperatures between Ventsim and Multiflux is shown in Figure A3.8. The results are in excellent agreement with 0.08 °C RMS error of the difference. Table A3.3 summarizes the comparison data for branch end temperatures.

The results lead to the conclusion that Ventsim is comparing excellently with MF and can be used as a native solver in the EWS implementation.

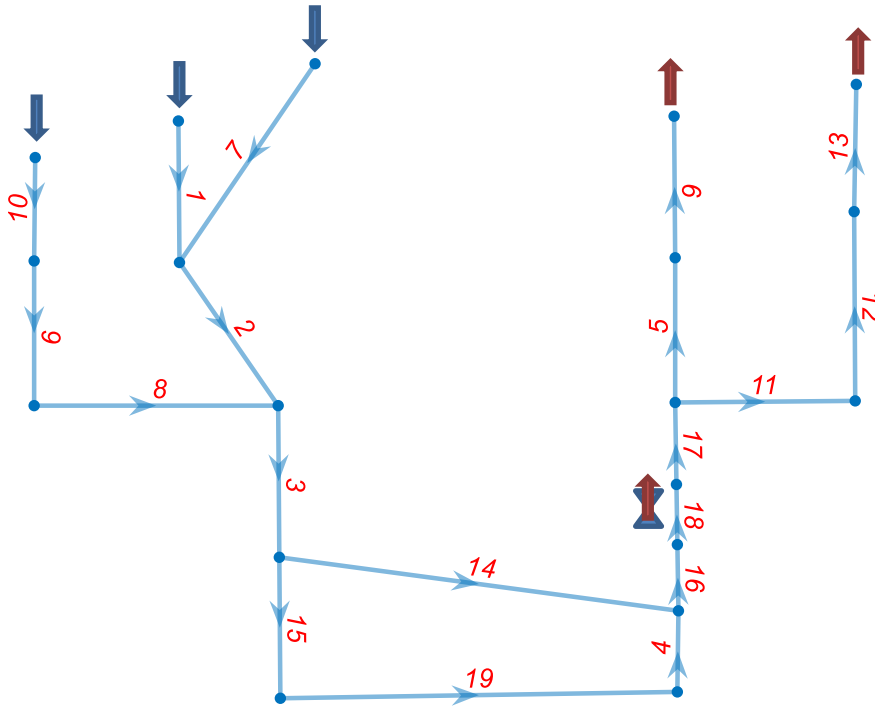


Figure A3.2. Branch ID assignment in MF.

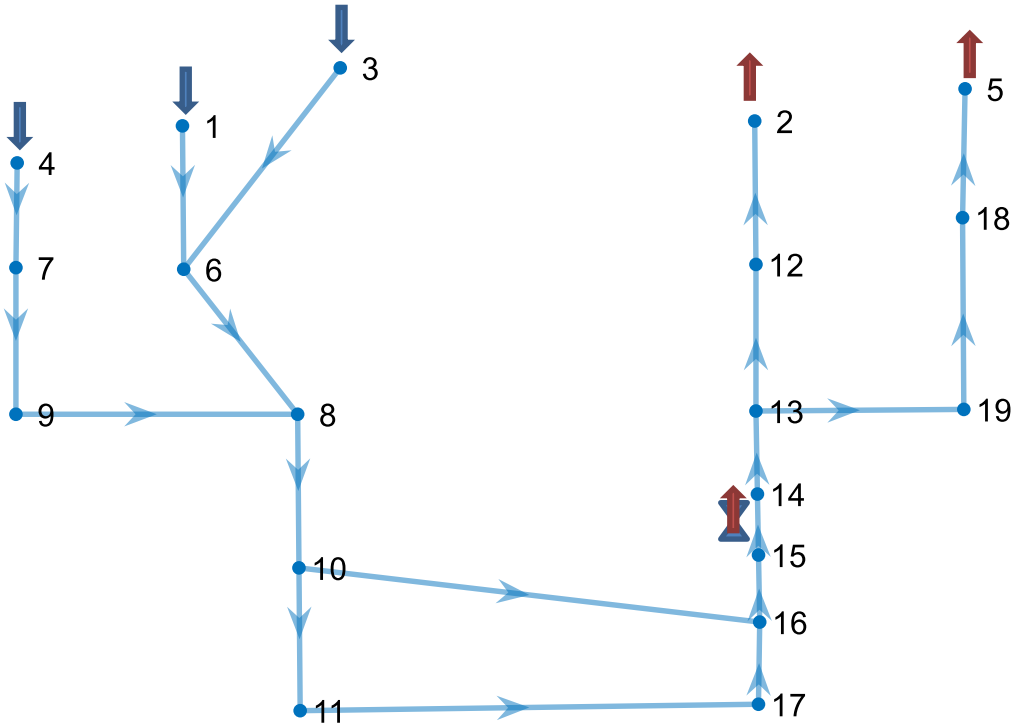


Figure A3.3. Node ID assignment in MF.

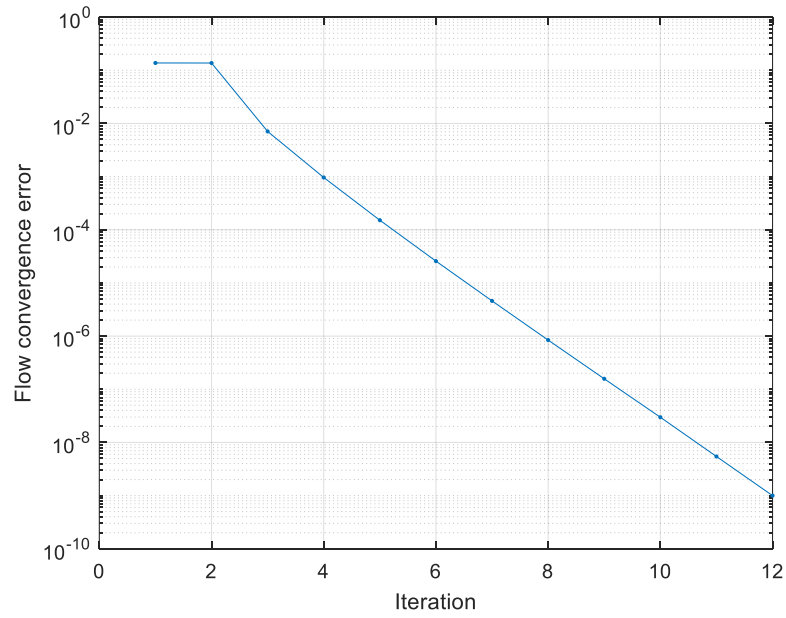


Figure A3.4. Flow solver convergence error.

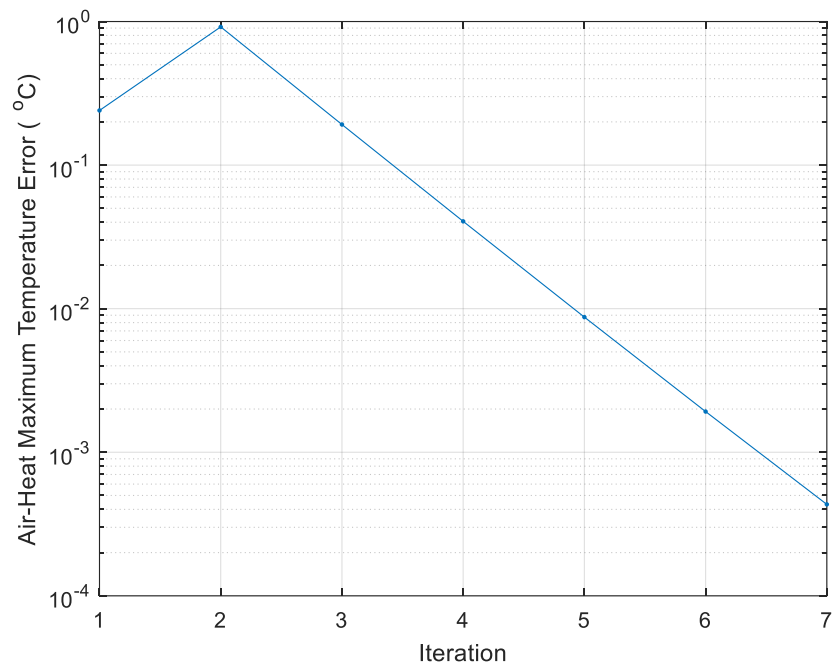


Figure A3.5. Coupled heat solver convergence error.

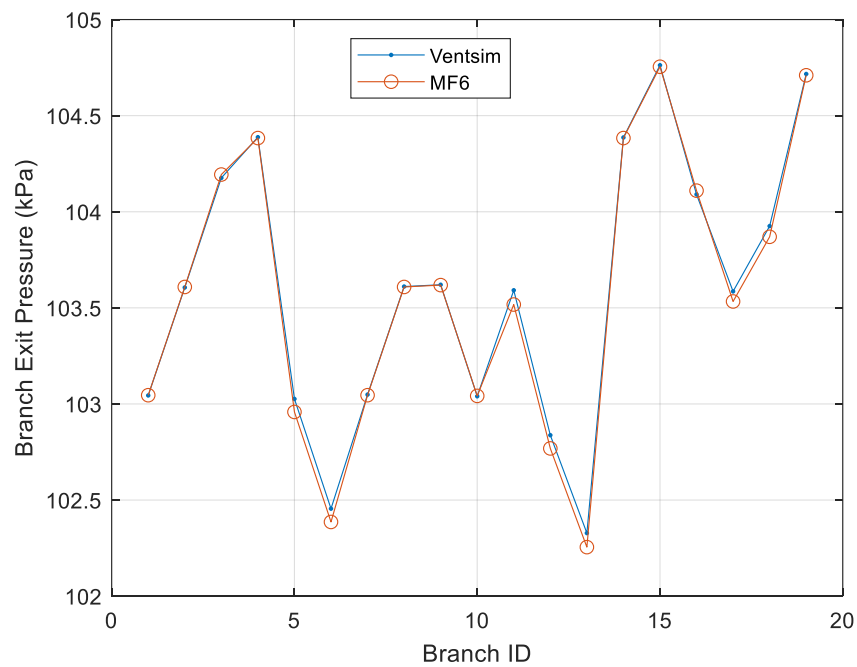


Figure A3.6. Comparison of branch end pressure between Ventsim and Multiflux, RMS= 40.3 Pa.

Table A3.1. Comparison data for branch end pressure between Ventsim and Multiflux.

Branch ID	Ventsim		Multiflux		Pressure Difference	
	P1 [kPa]	P2 [kPa]	P1 [kPa]	P2 [kPa]	DP1 [Pa]	DP2 [Pa]
1	102.48	103.04	102.48	103.05	0.0	1.3
2	103.04	103.61	103.05	103.61	5.8	2.7
3	103.59	104.18	103.61	104.19	20.9	17.6
4	104.72	104.39	104.71	104.38	-6.7	-4.6
5	103.61	103.03	103.53	102.96	-72.8	-67.7
6	103.03	102.46	102.96	102.39	-67.7	-69.1
7	102.25	103.05	102.25	103.05	0.0	-3.1
8	103.62	103.61	103.62	103.61	-1.9	-2.2
9	103.04	103.62	103.04	103.62	2.0	-1.9
10	102.63	103.04	102.63	103.04	0.0	2.0
11	103.61	103.59	103.53	103.52	-74.1	-74.2
12	103.59	102.84	103.52	102.77	-74.2	-68.9
13	102.84	102.33	102.77	102.26	-68.9	-73.0
14	104.20	104.39	104.19	104.38	-2.3	-3.0
15	104.20	104.76	104.19	104.75	-3.9	-7.9
16	104.37	104.09	104.38	104.11	17.0	19.7
17	103.93	103.59	103.87	103.53	-55.6	-52.4
18	104.09	103.93	104.11	103.87	19.7	-55.7
19	104.76	104.72	104.75	104.71	-7.9	-6.7

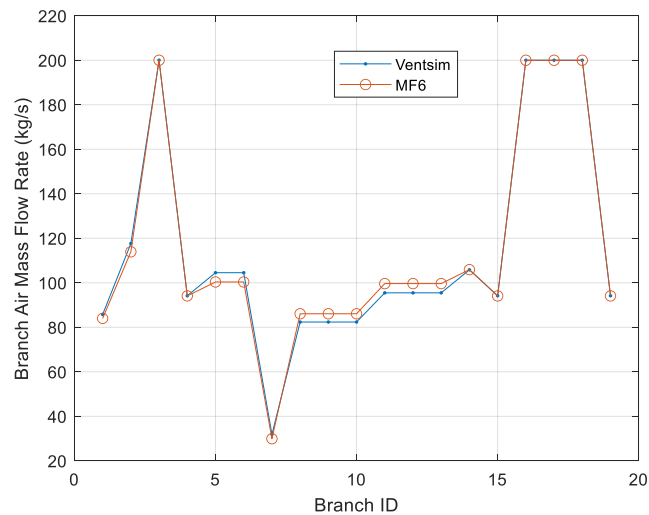
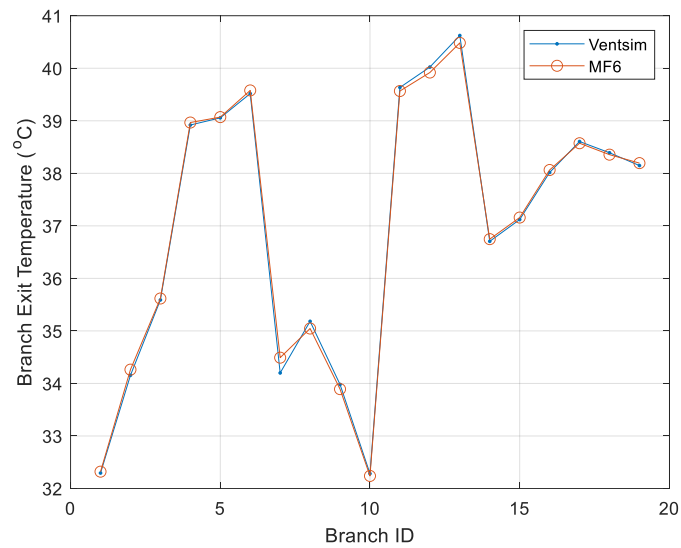


Figure A3.7. Comparison of branch airflow between Ventsim and Multiflux, RMS= 2.8 kg/s.

Table A3.2. Comparison data for branch airflow in kg/s between Ventsim and Multiflux.

Branch ID	Ventsim	Multiflux	Difference
1	85.75	84.00	-1.75
2	117.64	113.93	-3.71
3	200.00	200.00	0.00
4	94.16	94.10	-0.07
5	104.53	100.37	-4.16
6	104.53	100.37	-4.16
7	31.89	29.93	-1.96
8	82.36	86.07	3.71
9	82.36	86.07	3.71
10	82.36	86.07	3.71
11	95.47	99.63	4.16
12	95.47	99.63	4.16
13	95.47	99.63	4.16
14	105.84	105.90	0.07
15	94.16	94.10	-0.07
16	200.00	200.00	0.00
17	200.00	200.00	0.00
18	200.00	200.00	0.00
19	94.16	94.10	-0.07



RMS=0.08 °

Figure A3.8. Comparison of branch end temperatures between Ventsim and Multiflux, C.

Table A3.3. Comparison data for branch end temperatures between Ventsim and Multiflux.

Branch ID	Ventsim		Multiflux		Temperature Difference	
	T1 [°C]	T2 [°C]	T1 [°C]	T2 [°C]	DT1 [°C]	DT2 [°C]
1	30.65	32.29	30.65	32.32	0.00	-0.03
2	32.83	34.16	32.90	34.26	-0.07	-0.11
3	34.58	35.59	34.60	35.62	-0.02	-0.03
4	38.15	38.92	38.19	38.97	-0.05	-0.05
5	38.61	39.06	38.57	39.07	0.03	-0.01
6	39.06	39.52	39.07	39.58	-0.01	-0.06
7	30.52	34.20	30.52	34.49	0.00	-0.29
8	33.98	35.18	33.89	35.05	0.09	0.14
9	32.28	33.98	32.24	33.89	0.04	0.09
10	30.73	32.28	30.73	32.24	0.00	0.04
11	38.61	39.63	38.57	39.57	0.03	0.07
12	39.63	40.02	39.57	39.92	0.07	0.10
13	40.02	40.62	39.92	40.48	0.10	0.14
14	35.59	36.71	35.62	36.75	-0.03	-0.04
15	35.59	37.12	35.62	37.16	-0.03	-0.04
16	37.75	38.02	37.79	38.06	-0.04	-0.05
17	38.39	38.61	38.36	38.57	0.04	0.03
18	38.02	38.39	38.06	38.36	-0.05	0.04
19	37.12	38.15	37.16	38.19	-0.04	-0.05